

# 1 Norwegian Sea net community production estimated from O<sub>2</sub> 2 and prototype CO<sub>2</sub> optode measurements on a Seaglider

3 Luca Possenti<sup>1,5</sup>, Ingunn Skjelvan<sup>2</sup>, Dariia Atamanchuk<sup>3</sup>, Anders Tengberg<sup>4</sup>, Matthew P.  
4 Humphreys<sup>5</sup>, Socratis Loucaides<sup>6</sup>, Liam Fernand<sup>7</sup>, Jan Kaiser<sup>1</sup>

5 <sup>1</sup>Centre for Ocean and Atmospheric Sciences, School of Environmental Sciences, University of East Anglia,  
6 Norwich, UK

7 <sup>2</sup>NORCE Norwegian Research Centre, Bjerknes Centre for Climate Research, Bergen, Norway

8 <sup>3</sup>Dalhousie University, Halifax, Canada

9 <sup>4</sup>University of Gothenburg, Sweden

10 <sup>5</sup>NIOZ Royal Netherlands Institute for Sea Research, Department of Ocean Systems (OCS), Texel, the  
11 Netherlands

12 <sup>6</sup>National Oceanography Centre, European Way, Southampton, SO14 3ZH, UK

13 <sup>7</sup>Centre for Environment, Fisheries and Aquaculture Sciences, Lowestoft, UK, NR33 0HT

14 *Correspondence to:* Luca Possenti (luca.possenti@nioz.nl)

15 **Abstract.** We report on a pilot study using a CO<sub>2</sub> optode deployed on a Seaglider in the Norwegian Sea from  
16 March to October 2014. The optode measurements required drift- and lag-correction and in situ calibration using  
17 discrete water samples collected in the vicinity. We found that the optode signal correlated better with the  
18 concentration of CO<sub>2</sub>,  $c(\text{CO}_2)$ , than with its partial pressure,  $p(\text{CO}_2)$ . Using the calibrated  $c(\text{CO}_2)$  and a regional  
19 parameterisation of total alkalinity ( $A_T$ ) as a function of temperature and salinity, we calculated total dissolved  
20 inorganic carbon content,  $c(\text{DIC})$ , which had a standard deviation of 11  $\mu\text{mol kg}^{-1}$  compared with in situ  
21 measurements. The glider was also equipped with an oxygen (O<sub>2</sub>) optode. The O<sub>2</sub> optode was drift-corrected and  
22 calibrated using a  $c(\text{O}_2)$  climatology for deep samples. The calibrated data enabled the calculation of DIC- and  
23 O<sub>2</sub>-based net community production,  $N(\text{DIC})$  and  $N(\text{O}_2)$ . To derive  $N$ , DIC and O<sub>2</sub> inventory changes over time  
24 were combined with estimates of air-sea gas exchange, diapycnal mixing and entrainment of deeper waters.  
25 Glider-based observations captured two periods of increased Chl  $a$  inventory in late spring (May) and a second  
26 one in summer (June). For the May period, we found  $N(\text{DIC}) = (21 \pm 5) \text{ mmol m}^{-2} \text{ d}^{-1}$ ,  $N(\text{O}_2) = (94 \pm 16) \text{ mmol m}^{-2}$   
27  $\text{d}^{-1}$  and an (uncalibrated) Chl  $a$  peak concentration of  $c_{\text{raw}}(\text{Chl } a) = 3 \text{ mg m}^{-3}$ . During the June period,  $c_{\text{raw}}(\text{Chl } a)$   
28 increased to a summer maximum of 4  $\text{mg m}^{-3}$ , associated with  $N(\text{DIC}) = (85 \pm 5) \text{ mmol m}^{-2} \text{ d}^{-1}$  and  $N(\text{O}_2) =$   
29  $(126 \pm 25) \text{ mmol m}^{-2} \text{ d}^{-1}$ . The high-resolution dataset allowed for quantification of the changes in  $N$  before, during  
30 and after the periods of increased Chl  $a$  inventory. After the May period, the remineralisation of the material  
31 produced during the period of increased Chl  $a$  inventory decreased  $N(\text{DIC})$  to  $(-3 \pm 5) \text{ mmol m}^{-2} \text{ d}^{-1}$  and  $N(\text{O}_2)$  to  
32  $(0 \pm 2) \text{ mmol m}^{-2} \text{ d}^{-1}$ . The survey area was a source of O<sub>2</sub> and a sink of CO<sub>2</sub> for most of the summer. The  
33 deployment captured two different surface waters influence by the Norwegian Atlantic Current (NwAC) and the  
34 Norwegian Coastal Current (NCC). The NCC was characterised by lower  $c(\text{O}_2)$  and  $c(\text{DIC})$  than the NwAC, as

35 well as lower  $N(\text{O}_2)$  and  $c_{\text{raw}}(\text{Chl } a)$  but higher  $N(\text{DIC})$ . Our results show the potential of glider data to  
36 simultaneously capture time and depth-resolved variability in DIC and  $\text{O}_2$  concentrations.

## 37 **1 Introduction**

38 Climate models project an increase in the atmospheric  $\text{CO}_2$  mole fraction driven by anthropogenic emissions  
39 from a preindustrial value of  $280 \mu\text{mol mol}^{-1}$  (Neftel et al., 1982) to  $538\text{-}936 \mu\text{mol mol}^{-1}$  by 2100 (Pachauri and  
40 Reisinger, 2007). The ocean is known to be a major  $\text{CO}_2$  sink (Sabine et al., 2004; Le Quéré et al., 2009; Sutton  
41 et al., 2014); in fact, it has taken up approximately 25 % of this anthropogenic  $\text{CO}_2$  with a rate of  $(2.5\pm 0.6) \text{ Gt a}^{-1}$   
42 (in C equivalents) (Friedlingstein et al., 2019). This uptake alters the carbonate system of seawater and is causing  
43 a decrease in seawater pH, a process known as ocean acidification (Gattuso and Hansson, 2011). The processes  
44 affecting the marine carbonate system include air-sea gas exchange, photosynthesis and respiration, advection  
45 and vertical mixing, and  $\text{CaCO}_3$  formation and dissolution. For that reason, it is important to develop precise,  
46 accurate and cost-effective tools to observe  $\text{CO}_2$  trends, variability and related processes in the ocean. Provided  
47 that suitable sensors are available, autonomous ocean glider measurements may help resolve these processes.

48 To quantify the marine carbonate system, four variables are commonly measured: total dissolved inorganic  
49 carbon concentration,  $c(\text{DIC})$ ; total alkalinity,  $A_T$ ; the fugacity of  $\text{CO}_2$ ,  $f(\text{CO}_2)$ ; and pH. At thermodynamic  
50 equilibrium, knowledge of two of the four variables is sufficient to calculate the other two. Marine carbonate  
51 system variables are primarily measured on research ships, commercial ships of opportunity, moorings, buoys  
52 and floats (Hardman-Mountford et al., 2008; Monteiro et al., 2009; Takahashi et al., 2009; Olsen et al., 2016;  
53 Bushinsky et al., 2019). Moorings equipped with submersible sensors often provide limited vertical and  
54 horizontal, but good long-term temporal resolution (Hemsley, 2015). In contrast, ship-based surveys have higher  
55 vertical and spatial resolution than moorings but limited repetition frequency because of the expense of ship  
56 operations. Ocean gliders have the potential to replace some ship surveys because they are much cheaper to  
57 operate and will increase our coastal and regional observational capacity. However, the slow glider speed of  $1\text{-}2$   
58  $\text{km h}^{-1}$  only allows a smaller spatial coverage than ship surveys and the sensors require careful calibration to  
59 match the quality of data provided by ship-based sampling.

60 Carbonate system sensors suitable for autonomous deployment have been developed in the past decades, in  
61 particular pH sensors (Seidel et al., 2008; Martz et al., 2010; Rérolle et al., 2013) and  $p(\text{CO}_2)$  sensors  
62 (Atamanchuk et al., 2014; Bittig et al., 2012; Degrandpre, 1993; Goyet et al., 1992; Körtzinger et al., 1996). One  
63 of these sensors is the  $\text{CO}_2$  optode (Atamanchuk et al., 2014) which has been successfully deployed to monitor  
64 an artificial  $\text{CO}_2$  leak on the Scottish west coast (Atamanchuk, et al., 2015b), on a cabled underwater observatory  
65 (Atamanchuk et al., 2015a), to measure lake metabolism (Peeters et al., 2016), for fish transportation (Thomas et  
66 al., 2017) and on a moored profiler (Chu et al., 2020).

67  $c(\text{DIC})$  and  $c(\text{O}_2)$  measurements can be used to calculate net community production (NCP), which is defined as  
68 the difference between gross primary production (GPP) and community respiration (CR). At steady-state, NCP is  
69 equal to the rate of organic carbon export and transfer from the surface into the mesopelagic and deep waters  
70 (Lockwood et al., 2012). NCP is derived by vertical integration to a specific depth, that is commonly defined  
71 relative to the mixed layer depth ( $z_{\text{mix}}$ ) or the bottom of the euphotic zone (Plant et al., 2016). A system is  
72 defined as autotrophic when GPP is larger than CR (i.e. NCP is positive) and as heterotrophic when CR is larger  
73 than GPP (i.e. NCP is negative) (Ducklow and Doney, 2013).

74 NCP can be quantified using bottle incubations or in situ biogeochemical budgets (Sharples et al., 2006; Quay, et  
75 al, 2012; Seguro et al., 2019). Bottle incubations involve measuring production and respiration in vitro under  
76 dark and light conditions. Biogeochemical budgets combine O<sub>2</sub> and DIC inventory changes with estimates of air-  
77 sea gas exchange, entrainment, advection and vertical mixing (Neuer et al., 2007; Alkire et al., 2014; Binetti et  
78 al., 2020).

79 The Norwegian Sea is a complex environment due to the interaction between the Atlantic Water (NwAC)  
80 entering from the south-west, Arctic Water coming from the north and the Norwegian Coastal Current (NCC)  
81 flowing along the Norwegian coast (Nilsen and Falck, 2006). In particular, Atlantic Water enters the Norwegian  
82 Sea through the Faroe-Shetland Channel and Iceland-Faroe Ridge (Hansen and Østerhus, 2000) with salinity  $S$   
83 between 35.1 and 35.3 and temperatures ( $\theta$ ) warmer than 6 °C (Swift, 1986). The NCC water differs from the  
84 NwAC with a surface  $S < 35$  (Saetre and Ljoen, 1972) and a seasonal  $\theta$  signal (Nilsen and Falck, 2006).

85 Biological production in the Norwegian Sea varies during the year and 5 different periods can be discerned (Rey,  
86 2001): (1) winter with the smallest productivity and phytoplankton biomass; (2) a pre-bloom period; (3) the  
87 spring bloom when productivity increases and phytoplankton biomass reaches the annual maximum; (4) a post-  
88 bloom period with productivity mostly based on regenerated nutrients; (5) autumn with smaller blooms than in  
89 summer. Previous estimates of the DIC based net community production ( $N(\text{DIC})$ ) were based on discrete  
90  $c(\text{DIC})$  samples (Falck and Anderson, 2005) or were calculated from  $c(\text{O}_2)$  measurements and converted to C  
91 equivalents assuming Redfield stoichiometry of production/respiration (Falck and Gade, 1999; Skjelvan et al.,  
92 2001; Kivimäe, 2007). Glider measurements have been used to estimate NCP in other ocean regions (Nicholson  
93 et al., 2008; Alkire et al., 2014; Haskell et al., 2019; Binetti et al., 2020); however, as far as we know, this is the  
94 first study of net community production in the Norwegian Sea using a high-resolution glider dataset ( $>10^6$  data  
95 points; 40 s time resolution) and the first anywhere estimating NCP from a glider-mounted sensor directly  
96 measuring the marine carbonate system.

## 97 **2 Material and methods**

### 98 **2.1 List of symbols (unit)**

99	$A_T$	total alkalinity ( $\mu\text{mol kg}^{-1}$ )
100	$b$	backscatter signal (engineering units)
101	$c$	amount content ( $\mu\text{mol kg}^{-1}$ )
102	$C$	amount concentration ( $\text{mmol m}^{-3}$ )
103	Chl $a$	chlorophyll a
104	DIC	dissolved inorganic carbon
105	$E$	entrainment flux ( $\text{mmol m}^{-2} \text{d}^{-1}$ )
106	$F_V$	diapycnal eddy diffusion flux ( $\text{mmol m}^{-2} \text{d}^{-1}$ )
107	$f(\text{CO}_2)$	fugacity of CO <sub>2</sub> ( $\mu\text{atm}$ )
108	$I$	inventory ( $\text{mmol m}^{-2}$ )
109	$K_z$	diapycnal eddy diffusivity ( $\text{m}^2 \text{s}^{-1}$ )
110	$N$	net community production ( $\text{mmol m}^{-2} \text{d}^{-1}$ )
111	$p(\text{CO}_2)$	partial pressure of CO <sub>2</sub> ( $\mu\text{atm}$ )
112	$S$	practical salinity ()
113	$t$	time (s)

114	$U$	wind speed ( $\text{m s}^{-1}$ )
115	$x$	dry mole fraction ( $\text{mol mol}^{-1}$ )
116	$z_{\text{DCM}}$	depth of the deep chlorophyll maximum (m)
117	$z_{\text{lim}}$	integration depth (m)
118	$z_{\text{mix}}$	mixed layer depth (m)
119	$\Phi$	air-sea flux ( $\text{mmol m}^{-2} \text{d}^{-1}$ )
120	$\varphi$	$\text{CO}_2$ optode CalPhase ( $^\circ$ )
121	$\sigma_0$	potential density ( $\text{kg m}^{-3}$ )
122	$\theta$	Celsius temperature ( $^\circ\text{C}$ )
123	$\tau$	response time (s)
124		

## 125 2.2 Glider sampling

126 Kongsberg Seaglider 564 was deployed in the Norwegian Sea on 16 March 2014 at  $63.00^\circ \text{N}$ ,  $3.86^\circ \text{E}$  and  
 127 recovered on 30 October 2014 at  $62.99^\circ \text{N}$ ,  $3.89^\circ \text{E}$ . The Seaglider was equipped with a prototype Aanderaa  
 128 4797  $\text{CO}_2$  optode, an Aanderaa 4330F oxygen optode (Tengberg et al., 2006), a Seabird CTD and a combined  
 129 backscatter/chlorophyll  $a$  fluorescence sensor (Wetlabs Eco Puck BB2FLVMT). The mean sampling intervals  
 130 for each sensor varied with depth (Table 1).

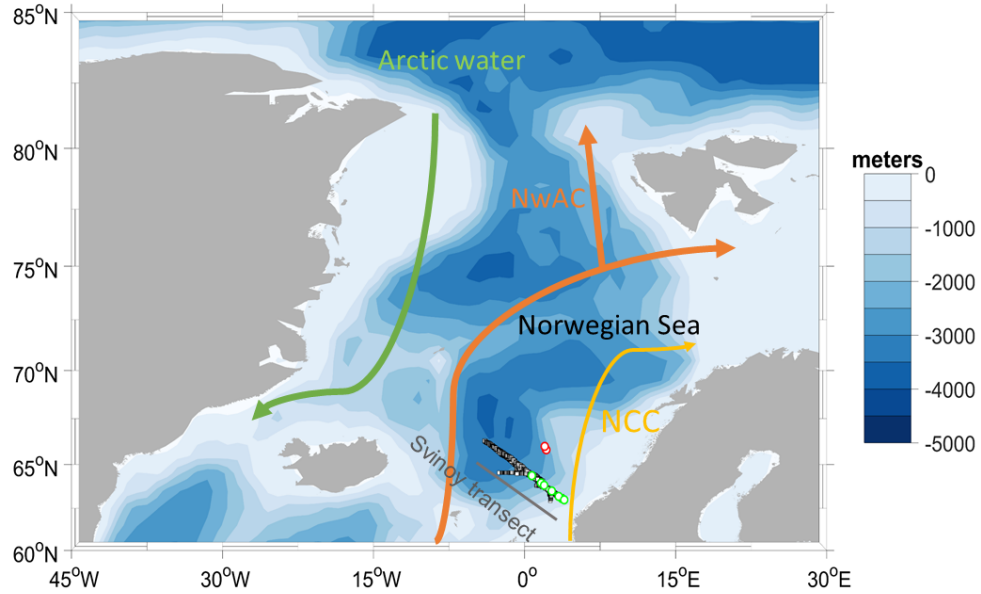
131 **Table 1.** Average sampling interval of Seabird CTD, Aanderaa 4330F oxygen optode, Aanderaa 4797  $\text{CO}_2$   
 132 optode and a combined backscatter/chlorophyll  $a$  fluorescence sensor (Wetlabs Eco Puck BB2FLVMT) in the  
 133 top 100 m, from 100 to 500 and from 500 to 1000 m.

Depth / m	$t(\text{CTD}) / \text{s}$	$t(\text{O}_2) / \text{s}$	$t(\text{CO}_2) / \text{s}$	$t(\text{Chl } a) / \text{s}$
0 – 100 m	24	49	106	62
100 – 500 m	31	153	233	-
500 – 1000 m	42	378	381	-

134

135 The deployment followed the Svinøy trench, from the open sea towards the Norwegian coast. The glider covered  
 136 a 536 km long transect 8 times (4 times in each direction) for a total of 703 dives (Figure 1).

137



138

139 **Figure 1:** Map of the glider deployment and the main currents. The black dots are the glider dives, the green and  
 140 the red dots are the water samples collected along the glider section and at Ocean Weather Station M (OWSM),  
 141 respectively. The three main water masses (Skjelvan et al., 2008) are the Norwegian Coastal Current (yellow),  
 142 the Norwegian Atlantic Current (NwAC, orange) and Arctic Water (green).

143

144

### 145 2.3 Discrete sampling

146 During the glider deployment, 70 discrete water samples from various depths (5, 10, 20, 30, 50, 100, 300, 500  
 147 and 1000 m) were collected on 5 different cruises on the R/V Haakon Mosby along the southern half of the  
 148 glider transect on 18 March, 5 May, 6 and 14 June, and 30 October 2014. Samples for  $c(\text{DIC})$  and  $A_T$  were  
 149 collected from 10 L Niskin bottles following the standard operational procedure (SOP) 1 of Dickson et al.  
 150 (2007). The  $c(\text{DIC})$  and  $A_T$  samples were preserved with saturated  $\text{HgCl}_2$  solution (final  $\text{HgCl}_2$  concentration: 15  
 151  $\text{mg dm}^{-3}$ ) and analysed within 14 days after the collection. Nutrient samples from the same Niskin bottles were  
 152 preserved with chloroform (Hagebo and Rey, 1984).  $c(\text{DIC})$  and  $A_T$  were analysed on shore according to SOP 2  
 153 and 3b (Dickson et al., 2007) using a VINDTA 3D (Marianda) with a CM5011 coulometer (UIC instruments)  
 154 and a VINDTA 3S (Marianda), respectively. The precision of the samples'  $c(\text{DIC})$  and  $A_T$  values was  $1 \mu\text{mol kg}^{-1}$   
 155 for both, based on duplicate samples and running Certified Reference Material (CRM) batch numbers 118 and  
 156 138 provided by professor A. Dickson, Scripps Institution of Oceanography, San Diego, USA (Dickson et al.,  
 157 2003). Nutrients were analysed on shore using an Alpkem Auto Analyzer. In addition, 43 water samples were  
 158 collected at Ocean Weather Station M (OWSM) on 5 different cruises on 22 March on R/V Haakon Mosby, on 9  
 159 May on R/V G.O. Sars, on 14 June on R/V Haakon Mosby, on 2 August and on 13 November 2014 on R/V  
 160 Johan Hjort from 10, 30, 50, 100, 200, 500, 800 and 1000 m depth. The OWSM samples were preserved and  
 161 analysed for  $A_T$  and  $c(\text{DIC})$  as the Svinøy samples. No phosphate and silicate samples were collected at OWSM.  
 162 Temperature ( $\theta$ ) and salinity ( $S$ ) profiles were measured at each station using a SeaBird 911 plus CTD. pH and  
 163  $f(\text{CO}_2)$  were calculated using the MATLAB toolbox CO2SYS (Van Heuven et al., 2011), with the following  
 164 constants:  $K_1$  and  $K_2$  carbonic acid dissociation constants of Lueker et al. (2000),  $K(\text{HSO}_4^-/\text{SO}_4^{2-})$  bisulfate

165 dissociation constant of Dickson (1990) and borate to chlorinity ratio of Lee et al. (2010). The precision of  $A_T$   
166 and  $c(\text{DIC})$  led to an uncertainty in the calculated  $c(\text{CO}_2)$  of  $0.28 \mu\text{mol kg}^{-1}$ . For the OWSM calculations, we  
167 used nutrient concentrations from the Svinøy section at a time as close as possible to the OWSM sampling as  
168 input. In the case of the glider, we derived a parameterisation for phosphate and silicate concentration as a  
169 function of sample depth and time. This parameterisation had an uncertainty of  $1.3$  and  $0.13 \mu\text{mol kg}^{-1}$  and a  $R^2$   
170 of  $0.6$  and  $0.4$ , for silicate and phosphate concentrations, respectively. The uncertainty was calculated as the root  
171 mean square difference between measured and parameterised concentrations. This nutrient concentration  
172 uncertainty contributed an uncertainty of  $0.04 \mu\text{mol kg}^{-1}$  in the calculation of  $c(\text{CO}_2)$ , which is negligible and  
173 smaller than the uncertainty caused by  $A_T$  and  $c(\text{DIC})$ .

## 174 2.4 Oxygen optode calibration

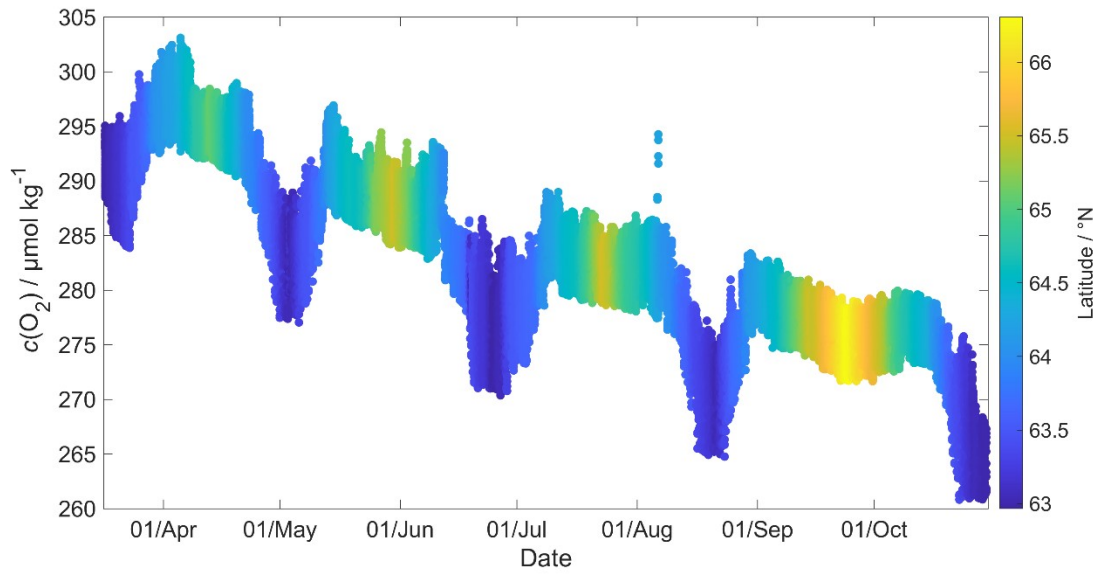
175 The last oxygen optode calibration before the deployment was performed in 2012 as a two-point calibration at  
176  $9.91 \text{ }^\circ\text{C}$  in air-saturated water and at  $20.37 \text{ }^\circ\text{C}$  in anoxic  $\text{Na}_2\text{SO}_3$  solution. Oxygen optodes are known to be  
177 affected by drift (Bittig et al., 2015), which is even worse for the fast-response foils used in the 4330F optode for  
178 glider deployments. It has been suggested that it is necessary to calibrate and drift correct the optode using  
179 discrete samples or in-air measurements (Nicholson and Feen, 2017). Unfortunately, no discrete samples were  
180 collected at glider deployment or recovery.

181 To overcome this problem, we used archived data to correct for oxygen optode drift. These archived  
182 concentration data (designated  $c_C(\text{O}_2)$ ) were collected at OWSM between 2001 and 2007 (downloaded from  
183 ICES data base) and in the glider deployment region between 2000 and 2018 (extracted from GLODAPv2;  
184 Olsen et al., 2016). To apply the correction, we used the oxygen samples corresponding to a potential density  $\sigma_0$   
185  $> 1028 \text{ kg m}^{-3}$  (corresponding to depths between 427 and 1000 m), because waters of these potential densities  
186 were always well below the mixed layer and therefore subject to limited seasonal and interannual variability, as  
187 evidenced by the salinity  $S$  and potential temperature  $\theta$  of these samples:  $S$  varied from  $34.88$  to  $34.96$ , with a  
188 mean of  $34.90 \pm 0.01$ ;  $\theta$  varied from  $0.45$  to  $-0.76 \text{ }^\circ\text{C}$ , with a mean of  $(-0.15 \pm 0.36) \text{ }^\circ\text{C}$ .

189 Figure 2 shows that the glider oxygen concentration ( $c_G(\text{O}_2)$ ) corresponding to  $\sigma_0 > 1028 \text{ kg m}^{-3}$  was  
190 characterised by two different water masses separated at a latitude of about  $64^\circ \text{ N}$ . We used the samples  
191 collected north of  $64^\circ \text{ N}$  to derive the glider optode correction because this reflects the largest area covered by  
192 the glider. We did not use the southern region because the archived samples from there covered only 5 days. For  
193 each day of the year with archived samples, we calculated the median concentration of the glider and the  
194 archived samples. Figure 3 shows a plot of the ratio between  $c_C(\text{O}_2)/c_G(\text{O}_2)$  against the day of the year and a  
195 linear fit, which is used to calibrate  $c_G(\text{O}_2)$  and correct for drift.

196 No lag correction was applied because the  $\text{O}_2$  optode had a fast response foil and showed no detectable lag ( $< 10$   
197 s), based on a comparison between descent and ascent profiles.

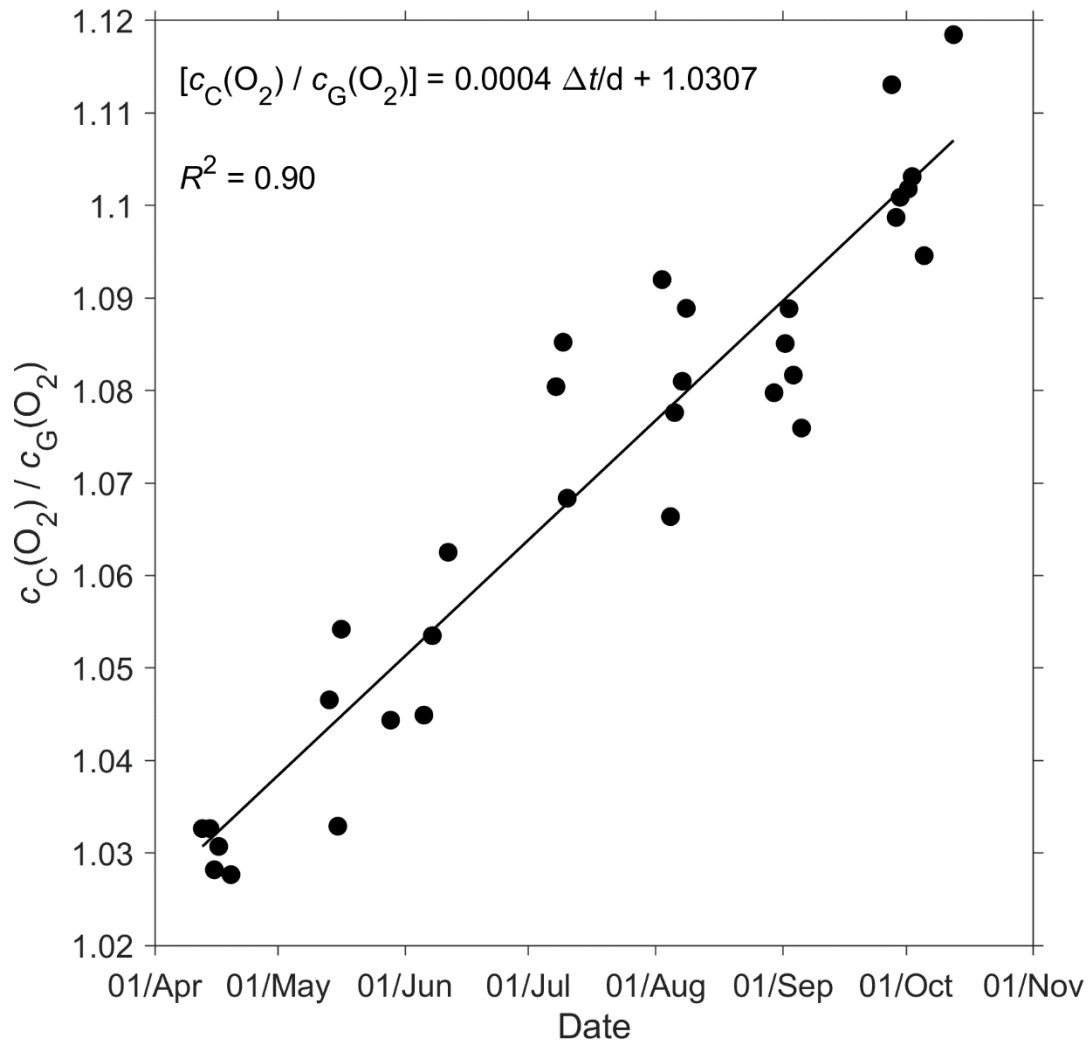
198



199

200

**Figure 2:** Glider oxygen concentration,  $c_G(O_2)$ , for  $\sigma_0 > 1028 \text{ kg m}^{-3}$  coloured by latitude.



201

202

203

204

205

**Figure 3:** A linear fit of the ratio between the daily median of the discrete oxygen samples ( $c_C(O_2)$ ) and glider oxygen data ( $c_G(O_2)$ ) for  $\sigma_0 > 1028 \text{ kg m}^{-3}$  was used to derive the  $c_C(O_2)$  drift and initial offset at deployment. The time difference  $\Delta t$  is calculated with respect to the deployment day on 16 March.

206 **2.5 CO<sub>2</sub> optode measurement principle**

207 The CO<sub>2</sub> optode consists of an optical and a temperature sensor incorporated into a pressure housing. The optical  
 208 sensor has a sensing foil comprising two fluorescence indicators (luminophores), one of which is sensitive to pH  
 209 changes and the other is not and thus used as a reference. The excitation and emission spectra of the two  
 210 fluorescence indicators overlap, but the reference indicator has a longer fluorescence lifetime than the pH  
 211 indicator. These two fluorescence lifetimes are combined using an approach known as Dual Lifetime  
 212 Referencing (DLR) (Klimant et al., 2001; von Bültzingslöwen et al., 2002). From the phase shift ( $\varphi$ ), the partial  
 213 pressure of CO<sub>2</sub>,  $p(\text{CO}_2)$ , is parameterised as an eight-degree polynomial (Atamanchuk et al., 2014):

214 
$$\log [p(\text{CO}_2)/\mu\text{atm}] = C_0 + C_1 \varphi + \dots + C_8 \varphi^8 \quad (1)$$

215 where  $C_0$  to  $C_8$  are temperature-dependent coefficients.

216 The partial pressure of CO<sub>2</sub> is linked to the CO<sub>2</sub> concentration,  $c(\text{CO}_2)$ , and the fugacity of CO<sub>2</sub>,  $f(\text{CO}_2)$ , via the  
 217 following relationship:

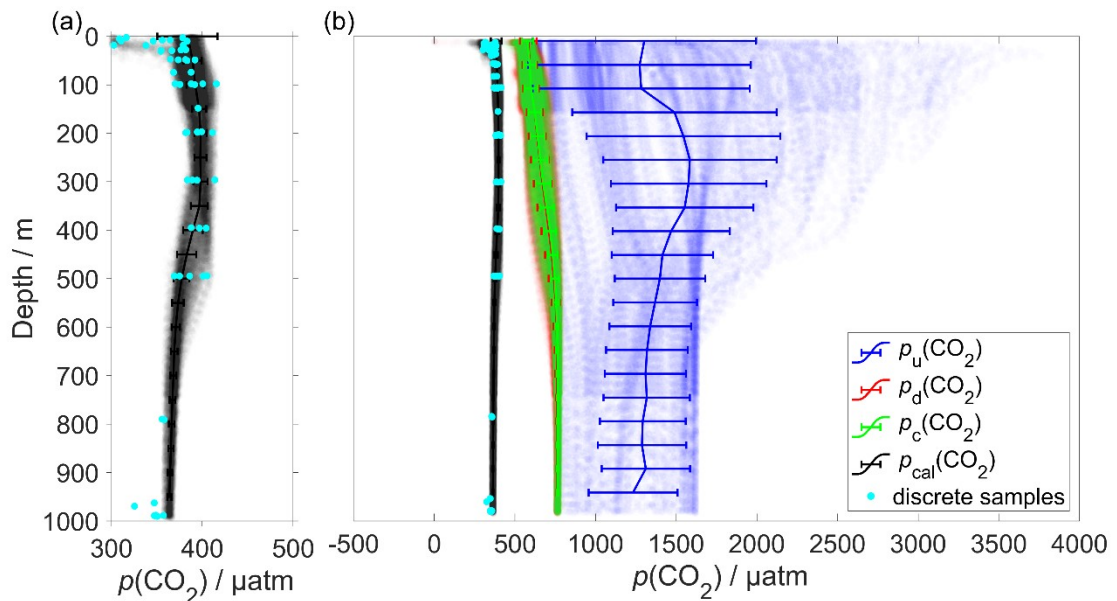
218 
$$c(\text{CO}_2) = p(\text{CO}_2) / [1 - p(\text{H}_2\text{O}) / p] \quad F(\text{CO}_2) = K_0(\text{CO}_2) f(\text{CO}_2) \quad (2)$$

219 where  $F(\text{CO}_2)$  is the solubility function (Weiss and Price, 1980),  $p(\text{H}_2\text{O})$  is the water vapour pressure,  $p$  is the  
 220 total gas tension (assumed to be near 1 atm) and  $K_0(\text{CO}_2)$  is the solubility coefficient.  $F$  and  $K_0$  vary according to  
 221 temperature and salinity.

222 **2.6 CO<sub>2</sub> optode lag and drift correction and calibration**

223 The CO<sub>2</sub> optode was fully functional between dives 31 (on 21 March 2014) and 400 (on 24 July 2014). After  
 224 dive 400, the CO<sub>2</sub> optode stopped sampling in the top 150 m. Figure 4 shows the outcome of each calibration  
 225 step: 0) uncalibrated optode output (blue dots), 1) drift correction (red dots), 2) lag correction (green dots) and 3)  
 226 calibration using discrete water samples (black dots).

227



228

229 **Figure 4:** Panel a) shows in black the calibrated  $p(\text{CO}_2)$  ( $p_{\text{cal}}(\text{CO}_2)$ ) and in azure the discrete samples. b) Plot of  
 230  $p(\text{CO}_2)$  versus depth where the vertical continuous lines are the mean every 50 m and the error bars represent the



231 standard deviation. Blue colour shows  $p_u(\text{CO}_2)$  without any correction; red shows  $p_d(\text{CO}_2)$  corrected for drift,  
 232 green represents  $p_c(\text{CO}_2)$  corrected for drift and lag; black shows  $p_{\text{cal}}(\text{CO}_2)$  calibrated against water samples  
 233 (azure dots) collected during the deployment (section 2.6).  $p_{\text{cal}}(\text{CO}_2)$  had a mean standard deviation of 22  $\mu\text{atm}$   
 234 and a mean bias of 1.8  $\mu\text{atm}$  compared with the discrete samples.

235

236 In order to correct for the drift occurring during the glider mission, we selected the  $\text{CO}_2$  optode measurements in  
 237 water with  $\sigma_0 > 1028 \text{ kg m}^{-3}$  (just as for  $\text{O}_2$ ; section 2.4). We calculated the median of the raw optode phase shift  
 238 data ("CalPhase"  $\varphi_{\text{cal}}$ ) for each Seaglider dive. Then, we calculated a drift coefficient ( $m_i$ ) as the ratio between  
 239 the median  $\varphi_{\text{cal}}$  for a given dive divided by the median  $\varphi_{\text{cal}}$  of dive 31. Drift-corrected  $\varphi_{\text{cal,d}}$  values were  
 240 calculated by dividing the raw  $\varphi_{\text{cal}}$  by the specific  $m_i$  for each dive.

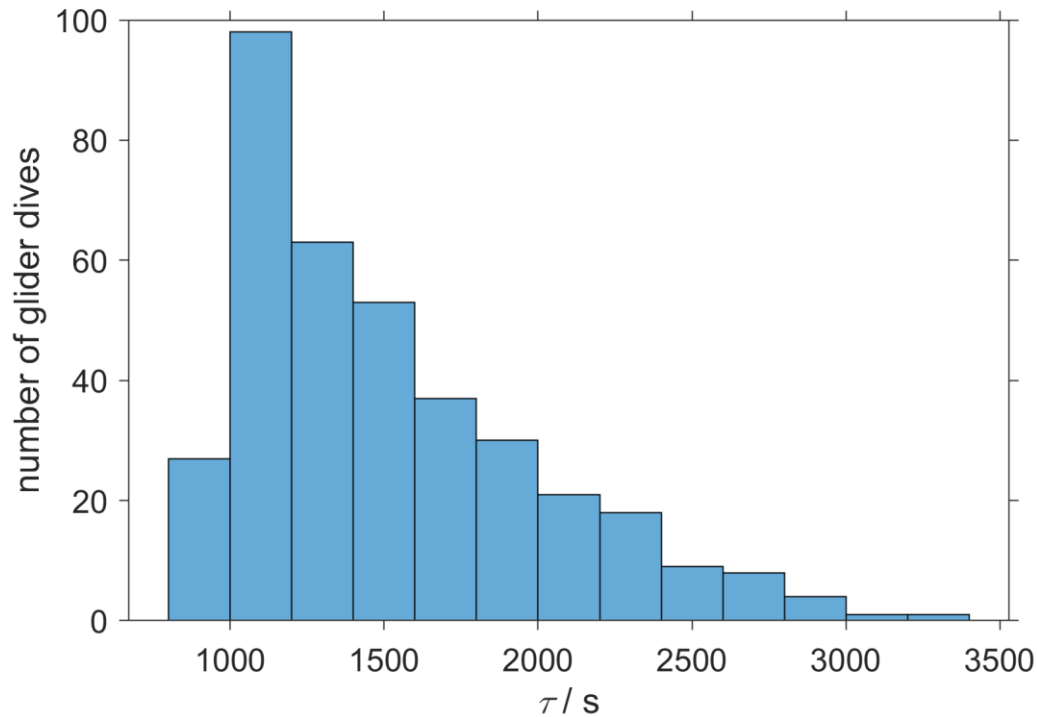
241 The  $\text{CO}_2$  optode was also affected by lag (Atamanchuk et al., 2014) caused by the slow response of the optode to  
 242 ambient  $c(\text{CO}_2)$  changes in time and depth. The lag created a discrepancy between the depth profiles obtained  
 243 during glider ascents and descents. To correct for this lag we applied the method of Miloshevich et al. (2004),  
 244 which was previously used by Fiedler et al. (2013) and Atamanchuk et al. (2015b) to correct the lag of the  
 245 Contros HydroC  $\text{CO}_2$  sensor (Fiedler et al., 2013; Saderne et al., 2013). This  $\text{CO}_2$  sensor has a different  
 246 measurement principle (infrared absorption) than the  $\text{CO}_2$  optode, but both rely on the diffusion of  $\text{CO}_2$  through  
 247 a gas-permeable membrane.

248 To apply the lag correction, the sampling interval ( $\Delta t$ ) needs to be sufficiently small compared to the sensor  
 249 response time ( $\tau$ ) and the ambient variability (Miloshevich, 2004). Before the lag correction,  $\varphi_{\text{cal,d}}$  was smoothed  
 250 to remove any outliers and "kinks" in the profile using the Matlab function rLOWESS. The smoothing function  
 251 applies a local regression every 9 points using a weighted robust linear least-squares fit. Subsequently,  $\tau$  was  
 252 determined such that the following lag-correction equation (Miloshevich, 2004) minimised the  $\varphi_{\text{cal,d}}$  difference  
 253 between each glider ascent and the following descent:

$$254 \quad p_c(\text{CO}_2, t_1) = \frac{p_d(\text{CO}_2, t_1) - p_d(\text{CO}_2, t_0) e^{-\Delta t/\tau}}{1 - e^{-\Delta t/\tau}} \quad (3)$$

255 where  $p_d(\text{CO}_2, t_0)$  is the drift-corrected value measured by the optode at time  $t_0$ ,  $p_d(\text{CO}_2, t_1)$  is the measured value  
 256 at time  $t_1$ ,  $\Delta t$  is the time between  $t_0$  and  $t_1$ ,  $\tau$  is the response time, and  $p_c(\text{CO}_2, t_1)$  is the lag-corrected value at  $t_1$ .

257 We calculated a  $\tau$  value for each glider dive and used the median of  $\tau$  (1384 s, 25<sup>th</sup> quartile: 1101 s; 75<sup>th</sup> quartile:  
 258 1799 s) (Figure 5), which was larger than  $\Delta t$  (258 s) and therefore met the requirement to apply the Miloshevich  
 259 (2004) method. To apply the lag correction the glider needs to sample same water mass during the ascent and  
 260 descent. The difference between the ascent and descent was minimal because was  $(0.13 \pm 0.33) ^\circ\text{C}$  for  $\theta$  and  
 261  $0.02 \pm 0.04$  for  $S$ . This lag correction reduced the average difference between glider ascent and descent from  
 262  $(71 \pm 30) \mu\text{atm}$  to  $(21 \pm 26) \mu\text{atm}$ .

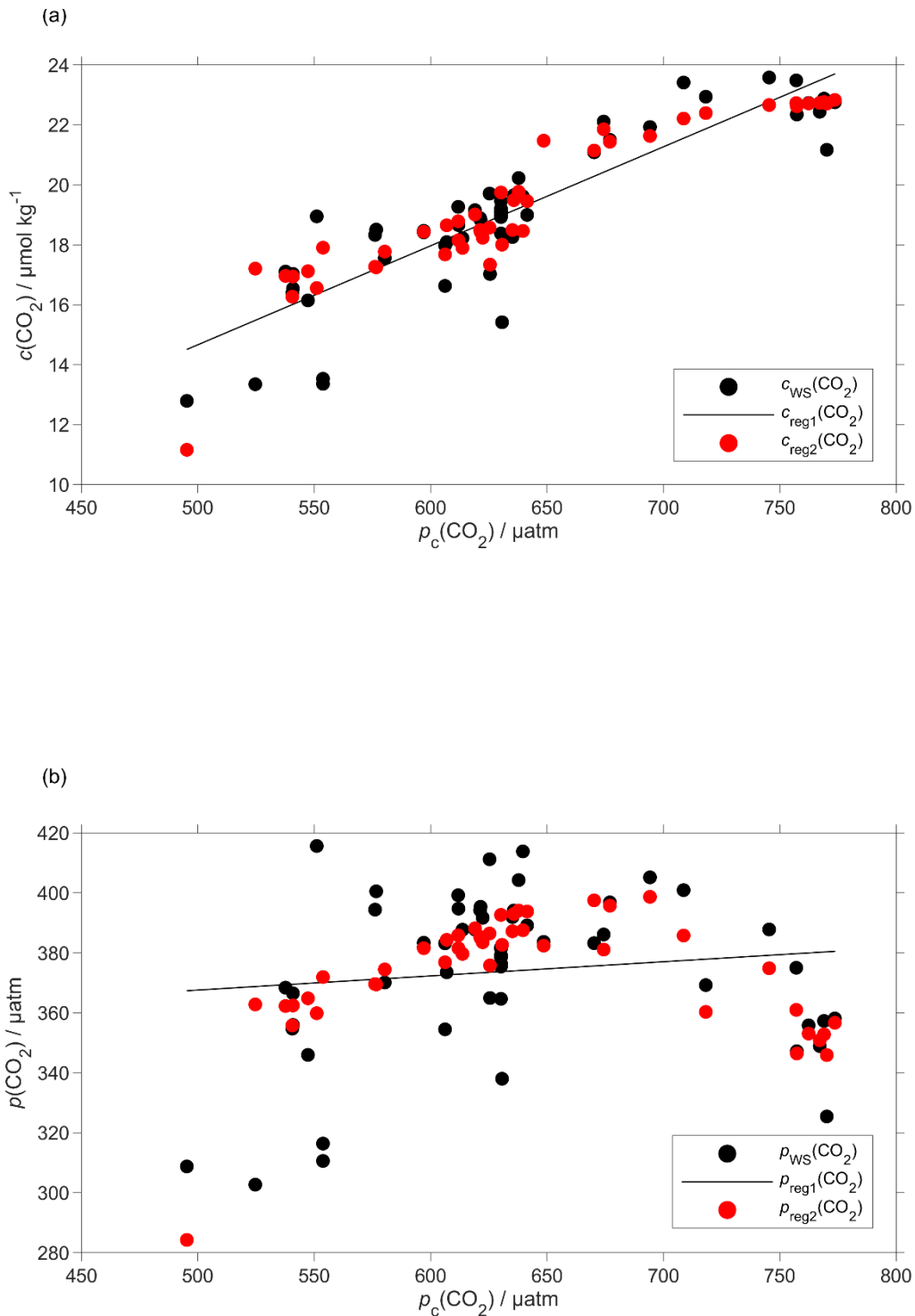


263

264 **Figure 5:** The histogram shows the distribution of the  $\tau$  calculated from glider dive 31 to 400 to correct the CO<sub>2</sub>  
 265 optode drift using the algorithm of Miloshevich (2004).

266 The CO<sub>2</sub> optode output was calibrated using the discrete samples collected throughout the mission. Using the  
 267 discrete sample time and potential density  $\sigma_0$ , we selected the closest CO<sub>2</sub> optode output. A linear regression  
 268 between optode output and  $c(\text{CO}_2)$  from the discrete samples ( $c_{\text{WS}}(\text{CO}_2)$ ) was used to calibrate the optode output  
 269  $p_c(\text{CO}_2)$  in terms of  $c(\text{CO}_2)$ .  $c(\text{CO}_2)$  had a better correlation than  $p(\text{CO}_2)$  ( $R^2 = 0.77$  vs.  $R^2 = 0.02$ ).

270 Plotting the regression residuals ( $c_r(\text{CO}_2)$ , calculated as the difference between  $c_{\text{WS}}(\text{CO}_2)$  and the value predicted  
 271 by the regression) revealed a quadratic relation between the regression residuals and water temperature ( $\theta$ ). We  
 272 have therefore included  $\theta$  and  $\theta^2$  in the optode calibration (Figure 6a). This second calibration increased the  
 273 correlation coefficient  $R^2$  from 0.77 to 0.90 and decreased the standard deviation of the regression residuals from  
 274 1.3 to 0.8  $\mu\text{mol kg}^{-1}$ . Even with the explicit inclusion of temperature in the calibration, the CO<sub>2</sub> optode response  
 275 remained more closely related to  $c(\text{CO}_2)$  than  $p(\text{CO}_2)$  (Figure 6b).



276

277 **Figure 6:** Regression (black lines, reg1) of the CO<sub>2</sub> optode output  $p_c(\text{CO}_2)$  against a) co-located concentration  
 278  $c_{\text{WS}}(\text{CO}_2)$  that has an uncertainty of  $0.28 \mu\text{mol kg}^{-1}$  b) and partial pressure  $p_{\text{WS}}(\text{CO}_2)$  of CO<sub>2</sub> in discrete water  
 279 samples (black dots). Also shown are the values predicted by including  $\theta$  and  $\theta^2$  in the regression used for optode  
 280 calibration (red dots, reg2). The regression equations are:

281 a) reg1:  $c_{\text{WS}}(\text{CO}_2) / (\mu\text{mol kg}^{-1}) = (0.033 \pm 0.003) p_c(\text{CO}_2) / \mu\text{atm} - 1.8 \pm 1.6$  ( $R^2 = 0.77$ )

282 a) reg2:  $c_{\text{WS}}(\text{CO}_2) / (\mu\text{mol kg}^{-1}) = (0.12 \pm 0.14) \theta / ^\circ\text{C} - (0.071 \pm 0.011) (\theta / ^\circ\text{C})^2 + (0.0094 \pm 0.0048) p_c(\text{CO}_2) / \mu\text{atm} + 16 \pm 4$   
 283 ( $R^2 = 0.90$ ).

284 b) reg1:  $p_{\text{WS}}(\text{CO}_2) / \mu\text{atm} = (0.05 \pm 0.05) p_c(\text{CO}_2) / \mu\text{atm} + 344 \pm 33$  ( $R^2 = 0.02$ )

285 b) reg2:  $p_{\text{WS}}(\text{CO}_2) / \mu\text{atm} = (21 \pm 3) \theta / ^\circ\text{C} - (1.9 \pm 0.2) (\theta / ^\circ\text{C})^2 + (0.2 \pm 0.1) p_c(\text{CO}_2) / \mu\text{atm} + 209 \pm 76$  ( $R^2 = 0.60$ ).

286

## 287 **2.7 Regional algorithm to estimate $A_T$**

288 To calculate  $c(\text{DIC})$ , we used two variables: (1) glider  $c(\text{CO}_2)$  derived as described in section 2.6 and (2)  $A_T$   
289 derived using a regional algorithm based on  $S$  and  $\theta$  depths of less than 1000 m. The algorithm followed the  
290 approach of Lee et al. (2006) and was derived using 663 water samples collected at OWSM from 2004 to 2014  
291 and GLODAPv2 (Olsen et al., 2016) data from the year 2000 in the deployment region. Discrete samples with  $S$   
292  $< 33$  were removed because these values were lower than the minimum  $S$  measured by the glider. The derived  $A_T$   
293 parameterisation is:

$$294 A_{T,\text{reg}} / (\mu\text{mol kg}^{-1}) = 2317.03 + 33.12 (S-35) + 7.94 (S-35)^2 + 0.96 (\theta/^\circ\text{C}-20) + 0.01 (\theta/^\circ\text{C}-20)^2 \quad (4)$$

295 The parameterisation has an uncertainty of  $8.2 \mu\text{mol kg}^{-1}$  calculated as the standard deviation of the residual  
296 difference between actual and parameterised  $A_T$ .

297 To test this parameterisation, we compared the predicted  $A_{T,\text{reg}}$  values with discrete measurements ( $A_{T,\text{WS}}$ )  
298 collected close in terms of time, potential density ( $\sigma_\theta$ ) and distance to the glider transect ( $n = 60$ ). These discrete  
299 samples and the glider had mean temperature and salinity differences of  $(0.17 \pm 0.68) ^\circ\text{C}$  and  $0.03 \pm 0.013$ ,  
300 respectively. The mean difference between  $A_{T,\text{WS}}$  and  $A_{T,\text{reg}}$  was  $(2.1 \pm 6.5) \mu\text{mol kg}^{-1}$ .

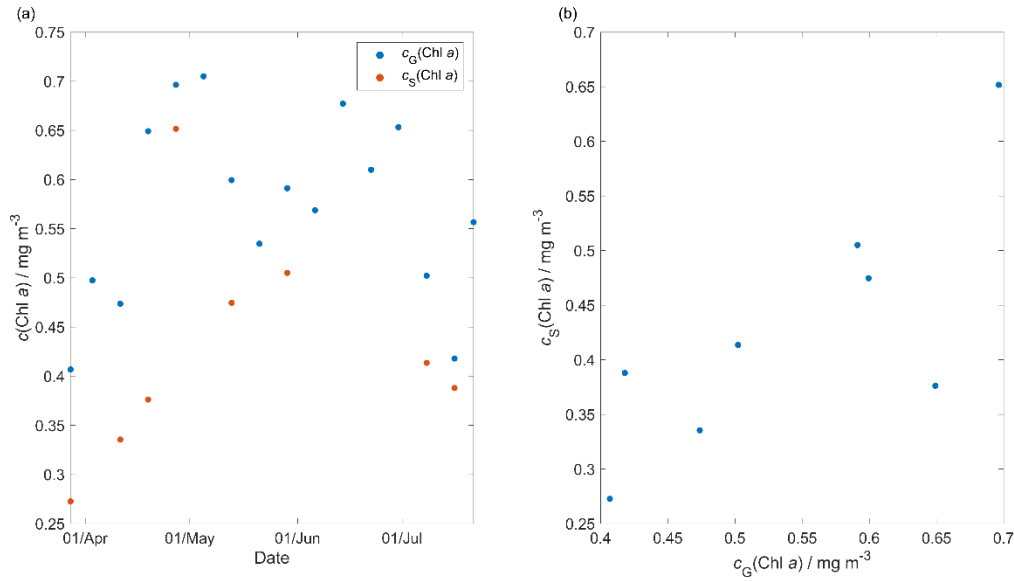
301 This  $A_T$  parameterisation was used in CO2SYS (Van Heuven et al., 2011) to calculate  $c(\text{DIC})$  from  $A_{T,\text{reg}}$  and the  
302 calibrated  $c(\text{CO}_2)$ ,  $c_{G,\text{cal}}(\text{CO}_2)$ . These calculated  $c_{G,\text{cal}}(\text{DIC})$  values were compared with  $c_{\text{WS}}(\text{DIC})$  of the same set  
303 of discrete samples used to calibrate  $c_{G,\text{cal}}(\text{CO}_2)$ , the only difference being that instead of the actual total  
304 alkalinity of the water sample ( $A_{T,\text{WS}}$ ), we used  $A_{T,\text{reg}}$ . The mean difference between  $c_{G,\text{cal}}(\text{DIC})$  and  $c_{\text{WS}}(\text{DIC})$   
305 was  $(3 \pm 11) \mu\text{mol kg}^{-1}$ , with the non-zero bias and the standard deviation due to the uncertainties in the  $A_{T,\text{reg}}$   
306 parameterisation and the  $c_{G,\text{cal}}(\text{CO}_2)$  calibration.

## 307 **2.8 Quality control of other measurement variables**

308 The thermal lag of the glider conductivity sensor was corrected using the method of Gourcuff (2014). Single-  
309 point outliers in conductivity were removed and replaced by linear interpolation. The glider CTD salinity was  
310 affected by presumed particulate matter stuck in the conductivity cell (Medeot et al., 2011) during dives 147,  
311 234, 244, 251, 272, 279, 303, 320 and 397 and sensor malfunction caused a poor match between glider ascent  
312 and descent during a dives 214, 215, 235 and 243. These dives were removed from the subsequent analysis.

313 Glider-reported chlorophyll concentrations,  $c_{\text{raw}}(\text{Chl } a)$ , were computed using the factory coefficients.  $c_{\text{raw}}(\text{Chl } a)$   
314 was affected by photochemical quenching during the daytime dives. To correct for quenching, we used the  
315 method of Hemsley et al. (2015) based on the night-time relationship between fluorescence and optical  
316 backscatter. This relationship was established in the top 60 meters and the night-time values were selected  
317 between sunset and sunrise. We calculated a linear fit between  $c_{\text{raw}}(\text{Chl } a)$  measured at night,  $c_{\text{N}}(\text{Chl } a)$ , and the  
318 backscatter signal measured at night ( $b_{\text{N}}$ ). The slope and the intercept were then used to derive corrected daytime  
319  $c_{\text{D}}(\text{Chl } a)$ . The glider-reported chlorophyll concentration has not been calibrated against in situ samples and is  
320 not expected to be accurate, even after correction for quenching. However, it should give an indication of the  
321 depth of the deep chlorophyll concentration maximum ( $z_{\text{DCM}}$ ) and the direction of chlorophyll concentration  
322 change (up/down). 8 day-means of  $c_{\text{raw}}(\text{Chl } a)$  were compared with satellite 8 day-composite chlorophyll

323 concentration (Figure 7) from Ocean Colour CCI (<https://esa-oceancolour-cci.org/>) and gave a mean  
 324 difference of  $(0.12 \pm 0.08) \text{ mg m}^{-3}$ .



325  
 326 **Figure 7:** Comparison between the 8 day-glider  $c(\text{Chl } a)$  ( $c_G(\text{Chl } a)$ ) mean and the 8 day-satellite  $c(\text{Chl } a)$   
 327 ( $c_S(\text{Chl } a)$ ) download from Ocean Colour CCI (<https://esa-oceancolour-cci.org/>), as time-series (panel a) and  
 328 scatter plot (panel b).

### 329 2.9 Calculation of oxygen-based net community production $N(\text{O}_2)$

330 Calculating net community production  $N$  from glider data is challenging because the glider continuously moves  
 331 through different water masses. For that reason we subdivided the transect by binning the data into  $0.1^\circ$  latitude  
 332 intervals to derive  $\text{O}_2$  concentration changes every two transects. The changes were calculated between transects  
 333 in the same direction of glider travel (e.g. transects 1 and 3, both in N-S direction) to have approximately the  
 334 same time difference (40-58 days) at every latitude. If instead we had used two consecutive transects, this would  
 335 lead to a highly variable time difference of near-0 to about 50 days along the transect.

336 We calculated  $N(\text{O}_2)$  (in  $\text{mmol m}^{-2} \text{d}^{-1}$ ) from the oxygen inventory changes  $(\Delta I(\text{O}_2)/\Delta t)$  corrected for air-sea  
 337 exchange  $\Phi(\text{O}_2)$ , normalised to  $z_{\text{mix}}$  when  $z_{\text{mix}}$  was deeper than the integration depth of  $z_{\text{lim}}$ , entrainment  $E(\text{O}_2)$   
 338 and diapycnal eddy diffusion  $F_v(\text{O}_2)$ :

$$339 \quad N(\text{O}_2) = \frac{\Delta I(\text{O}_2)}{\Delta t} + \Phi(\text{O}_2) \frac{\min(z_{\text{lim}}, z_{\text{mix}})}{z_{\text{mix}}} - E(\text{O}_2) - F_v(\text{O}_2) \quad (5)$$

340 The inventory changes were calculated as the difference between two transects of the integrated oxygen  
 341 concentration  $C(\text{O}_2)$ .  $C(\text{O}_2)$  (in  $\text{mmol m}^{-3}$ ) was derived from the oxygen content  $c(\text{O}_2)$  (in  $\mu\text{mol kg}^{-1}$ ) by  
 342 multiplication with the water density (about  $1027 \text{ kg m}^{-3}$ , but we used the actual values). A default integration  
 343 depth of 45 m was chosen to capture the deepest extent of the deep chlorophyll maximum ( $z_{\text{DCM}}$ ) found during  
 344 the deployment, which likely represents the extent of the euphotic zone.

345 The inventory changes for every latitude bin were calculated using the following equation:

$$346 \quad \frac{\Delta I(\text{O}_2)}{\Delta t} = \frac{\int_0^{45 \text{ m}} C_{n+1}(\text{O}_2, z) dz - \int_0^{45 \text{ m}} C_n(\text{O}_2, z) dz}{t_{n+1} - t_n} \quad (6)$$

347 where  $n$  is the transect number,  $t$  is the day of the year and  $C(\text{O}_2, z)$  is the vertical  $\text{O}_2$  concentration profile.

348 The air-sea flux of oxygen,  $\Phi(\text{O}_2)$  was calculated for each glider dive using the median  $C(\text{O}_2)$ ,  $\theta$  and  $S$  in the top  
349 10 m. We followed the method of Woolf and Thorpe (1991) that includes the effect of bubble equilibrium  
350 supersaturation in the calculations:

$$351 \quad \Phi(\text{O}_2) = k_w(\text{O}_2) \{ (C(\text{O}_2) - [1 + \Delta_{\text{bub}}(\text{O}_2)] C_{\text{sat}}(\text{O}_2)) \} \quad (7)$$

352 where  $k_w(\text{O}_2)$  is the gas transfer coefficient,  $\Delta_{\text{bub}}(\text{O}_2)$  is the increase of equilibrium saturation due to bubble  
353 injection and  $C_{\text{sat}}(\text{O}_2)$  is the oxygen saturation.  $C_{\text{sat}}(\text{O}_2)$  was calculated from  $S$  and  $\theta$  using the solubility  
354 coefficients of Benson and Krause Jr (1984), as fitted by Garcia and Gordon (1992).  $\Delta_{\text{bub}}(\text{O}_2)$  was calculated  
355 from the following equation:

$$356 \quad \Delta_{\text{bub}}(\text{O}_2) = 0.01 \left( \frac{U}{U_0} \right)^2 \quad (8)$$

357 where  $U$  is 10 m-wind speed with 1 hour resolution (ECMWF ERA5,  
358 <https://www.ecmwf.int/en/forecasts/datasets/reanalysis-datasets/era5>) and  $U_0$  represents the wind speed when the  
359 oxygen concentration is 1 % supersaturated and has a value of  $9 \text{ m s}^{-1}$  (Woolf and Thorpe, 1991).  $U$  has a spatial  
360 resolution of  $0.25^\circ$  latitude and  $0.25^\circ$  longitude and was interpolated to the glider position at the beginning of the  
361 dive.

362 The transfer velocity  $k_w(\text{O}_2)$  was calculated based on Wanninkhof (2014):

$$363 \quad \frac{k_w(\text{O}_2)}{\text{cm h}^{-1}} = 0.251 \left( \frac{Sc(\text{O}_2)}{660} \right)^{-0.5} \left( \frac{U}{\text{m s}^{-1}} \right)^2 \quad (9)$$

364 The Schmidt number,  $Sc(\text{O}_2)$ , was calculated using the parameterisation of Wanninkhof (2014). To account for  
365 wind speed variability,  $k_w(\text{O}_2)$  applied to calculate  $N(\text{O}_2)$  was a weighted mean. This value was calculated using  
366 the varying daily-mean wind speed  $U$  in the time interval between  $t_n$  and  $t_{n+1}$  ( $\Delta t$ ) (50 days) using a 5 point-  
367 median  $z_{\text{mix}}$  (section 3.2) (Reuer et al., 2007). The time interval is the same as used to calculate  $\frac{\Delta I(\text{O}_2)}{\Delta t}$ .

368 The entrainment flux,  $E(\text{O}_2)$ , was calculated as the oxygen flux when the mixed layer depth deepens in time and  
369 is greater than  $z_{\text{lim}}$  at time  $t_2$ :

$$370 \quad E(\text{O}_2) = \frac{I(\text{O}_2, t_1, z_{\text{mix}}(t_2)) \frac{z_{\text{lim}}}{z_{\text{mix}}(t_2)} - I(\text{O}_2, t_1, z_{\text{lim}})}{t_2 - t_1} \quad (10)$$

371 where  $t_2 - t_1$  represents the change in time,  $z_{\text{mix}}$  is the mixed layer depth,  $I(\text{O}_2, t_1, z_{\text{mix}}(t_2))$ , is the expected  
372 inventory that would result from a mixed layer deepening to  $z_{\text{mix}}(t_2)$  between  $t_2$  and  $t_1$ , and  $I(\text{O}_2, t_1, z_{\text{lim}})$  is the  
373 original inventory at  $t_1$ .

374 The effect of diapycnal eddy diffusion ( $F_v$ ) was calculated at  $z_{\text{mix}}$  when it was deeper than  $z_{\text{lim}}$  and at  $z_{\text{lim}}$  when  
375  $z_{\text{mix}}$  was shallower than  $z_{\text{lim}}$ , using the following equation:

$$376 \quad F_v(\text{O}_2) = K_z \frac{\partial C(\text{O}_2)}{\partial z} \quad (11)$$

377 for a vertical eddy diffusivity ( $K_z$ ) of  $10^{-5} \text{ m}^2 \text{ s}^{-1}$  (Naveira Garabato et al., 2004). The effect of  $F_v(\text{O}_2)$  on  $N(\text{O}_2)$   
378 was negligible (Figure A2b) with a median of  $(-0.1 \pm 0.5) \text{ mmol m}^{-2} \text{ d}^{-1}$ .

379 **2.10 Calculation of dissolved inorganic carbon-based net community production,  $N(\text{DIC})$**

380  $N(\text{DIC})$  was expressed in  $\text{mmol m}^{-2} \text{d}^{-1}$  and was calculated from DIC inventory changes ( $\Delta I(\text{DIC})/\Delta t$ ), air-sea  
381 flux of  $\text{CO}_2$ ,  $\Phi(\text{CO}_2)$ , entrainment  $E(\text{DIC})$  and diapycnal diffusion  $F_v(\text{DIC})$ :

$$382 \quad N(\text{DIC}) = -\frac{\Delta(\text{DIC})}{\Delta t} - \Phi(\text{CO}_2) \frac{\min(z_{\text{lim}}, z_{\text{mix}})}{z_{\text{mix}}} + E(\text{DIC}) + F_v(\text{DIC}) \quad (12)$$

383 Firstly,  $\Phi(\text{CO}_2)$  was calculated using the 10 m wind speed with 1 hour resolution downloaded from ECMWF  
384 ERA5. As for oxygen, we selected the closest wind speed data point at the beginning of each glider dive. We  
385 used the monthly mean atmospheric  $\text{CO}_2$  dry mole fraction ( $x(\text{CO}_2)$ ) downloaded from the Greenhouse Gases  
386 Reference Network Site (<https://www.esrl.noaa.gov/gmd/ccgg/ggrn.php>) closest to the deployment at Mace  
387 Head, County Galway, Ireland (Dlugokencky et al., 2015). Using  $x(\text{CO}_2)$  we calculated the air-saturation  
388 concentration  $C_{\text{atm}}(\text{CO}_2)$ :

$$389 \quad C_{\text{atm}}(\text{CO}_2) = x(\text{CO}_2) p_{\text{baro}} F(\text{CO}_2) \quad (13)$$

390 where  $p_{\text{baro}}$  is the mean sea level pressure and  $F(\text{CO}_2)$  is the  $\text{CO}_2$  solubility function (in  $\text{mol dm}^{-3} \text{atm}^{-1}$ )  
391 calculated from surface  $\theta$  and  $S$  (Weiss and Price, 1980).

392 The seawater  $c(\text{CO}_2)$  at the surface was calculated using the median in the top 10 meters between the glider  
393 ascent and descent of the following dive  $c(\text{CO}_2)$ . From this,  $\Phi(\text{CO}_2)$  was calculated:

$$394 \quad \Phi(\text{CO}_2) = k(\text{CO}_2) [C(\text{CO}_2) - C_{\text{atm}}(\text{CO}_2)]. \quad (14)$$

395  $k(\text{CO}_2)$  was calculated using the parameterisation of Wanninkhof (2014):

$$396 \quad \frac{k_w(\text{CO}_2)}{\text{cm h}^{-1}} = 0.251 \left( \frac{Sc(\text{CO}_2)}{660} \right)^{-0.5} \left( \frac{U}{\text{m s}^{-1}} \right)^2 \quad (15)$$

397  $Sc(\text{CO}_2)$  is the dimensionless Schmidt number at the seawater temperature (Wanninkhof, 2014). To account for  
398 wind speed variability,  $k_w(\text{CO}_2)$  applied to calculate  $N(\text{DIC})$  was a weighted mean based on the varying daily-  
399 mean wind speed  $U$  in the time interval between  $t_n$  and  $t_{n+1}$  ( $\Delta t$ ) used to calculate  $\frac{\Delta I(\text{DIC})}{\Delta t}$  and for 40 50 days to  
400 calculate  $\Phi(\text{CO}_2)$  (section 3.2) (Reuer et al., 2007).

401 The DIC inventory changes were calculated in the top 45 m with the following equation:

$$402 \quad \frac{\Delta I(\text{DIC})}{\Delta t} = \frac{\int_0^{45 \text{ m}} c_{n+1}(\text{DIC}, z) dz - \int_0^{45 \text{ m}} c_n(\text{DIC}, z) dz}{t_{n+1} - t_n} \quad (16)$$

403 Just as for  $C(\text{O}_2)$ ,  $C(\text{DIC})$  (in  $\text{mmol m}^{-3}$ ) was derived from the DIC content  $c(\text{DIC})$  (in  $\mu\text{mol kg}^{-1}$ ) by  
404 multiplication with the water density (about  $1027 \text{ kg m}^{-3}$ , but we used the actual values).

405 The entrainment flux,  $E(\text{DIC})$ , was calculated as the DIC flux when the mixed layer depth deepens in time and is  
406 greater than  $z_{\text{lim}}$  at time  $t_2$ :

$$407 \quad E(\text{DIC}) = \frac{I(\text{DIC}, t_1, z_{\text{mix}}(t_2)) - I(\text{DIC}, t_1, z_{\text{lim}})}{t_2 - t_1} \quad (17)$$

408 As for oxygen, the effect of diapycnal eddy diffusion ( $F_v$ ) was calculated at  $z_{\text{mix}}$  when it was deeper than  $z_{\text{lim}}$  and  
409 at  $z_{\text{lim}}$  when  $z_{\text{mix}}$  was shallower than  $z_{\text{lim}}$ , using the following equation:

$$410 \quad F_v(\text{DIC}) = K_z \frac{\partial C(\text{DIC})}{\partial z} \quad (18)$$

411 for a  $K_z$  of  $10^{-5} \text{ m}^2 \text{ s}^{-1}$  (Naveira Garabato et al., 2004). The effect of  $F_v(\text{DIC})$  was negligible (Figure A2a) with a  
 412 median of  $(0.1 \pm 0.3) \text{ mmol m}^{-2} \text{ d}^{-1}$ .

413 The contribution of horizontal advection to  $N(\text{DIC})$  was considered minimal over the timescales we calculated  
 414 inventory changes because previous studies have shown that changes in  $C(\text{DIC})$  during summer are mainly  
 415 controlled by biology and air-sea interactions (Gislefoss et al., 1998). For that reason, previous studies that  
 416 estimated  $N$  in the Norwegian Sea have also neglected advective fluxes (Falck and Anderson, 2005; Falck and  
 417 Gade, 1999; Kivimäe, 2007; Skjelvan et al., 2001).

418 Uncertainties in  $N(\text{DIC})$  and  $N(\text{O}_2)$  were evaluated with a Monte-Carlo approach. The uncertainties of the input  
 419 variables are shown in Table 2; we repeated the analysis 1000 times. The total uncertainty in  $N$  was calculated as  
 420 the standard deviation of the 1000 Monte-Carlo simulations.

421 **Table 2.** Uncertainty associated with  $N(\text{DIC})$  and  $N(\text{O}_2)$  input variables calculated by a Monte Carlo approach

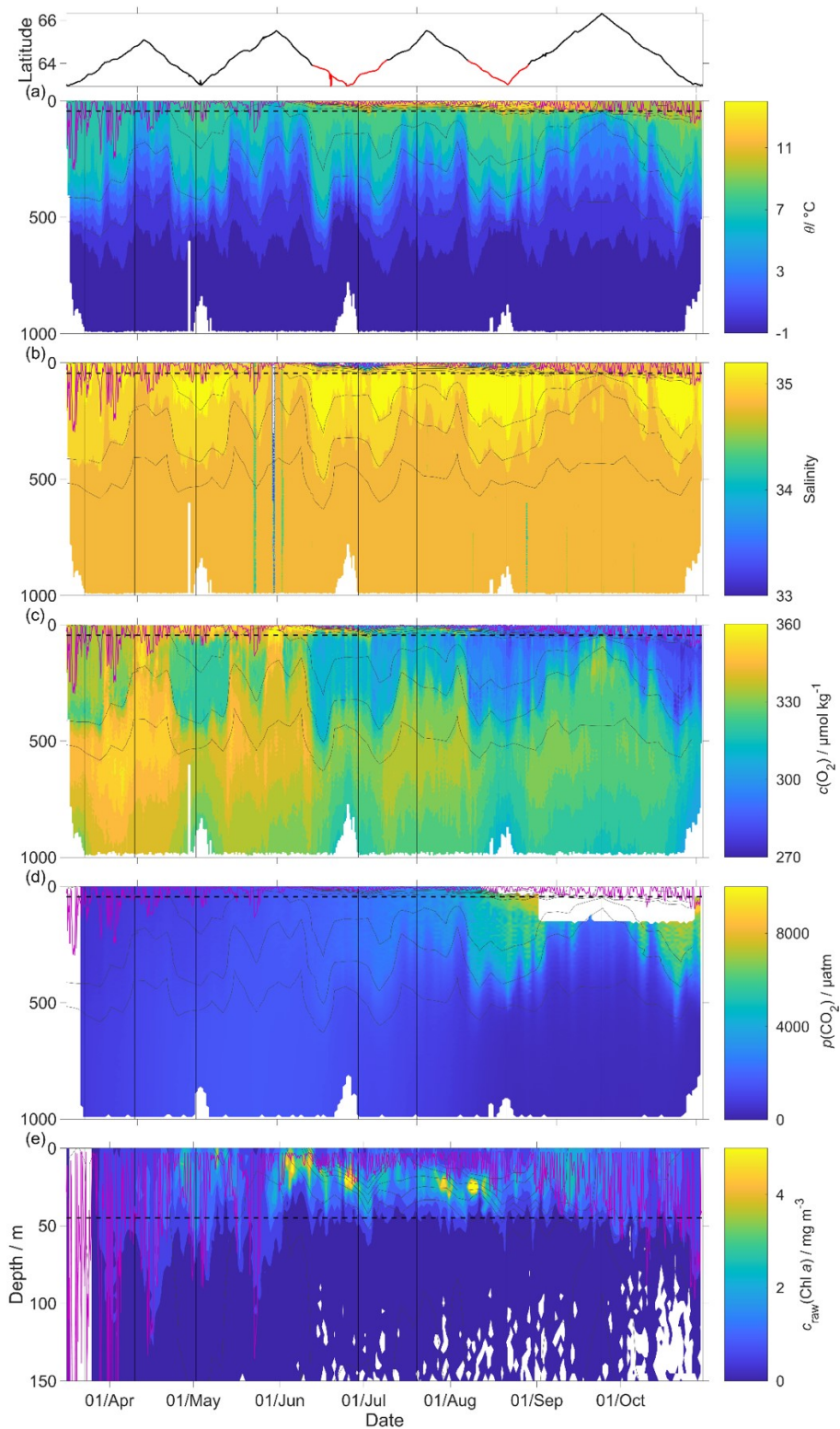
Variable	Error	Reference/Method
$c(\text{DIC})$	$11 \mu\text{mol kg}^{-1}$	Standard deviation of the differences to discrete water samples.
$S$	0.01	Standard deviation of glider salinities for $\sigma_0 > 1028 \text{ kg m}^{-3}$ and latitude $> 64^\circ \text{ N}$
$\theta$	$0.3 \text{ }^\circ\text{C}$	Standard deviation of glider temperature for $\sigma_0 > 1028 \text{ kg m}^{-3}$ and latitude $> 64^\circ \text{ N}$
$C_{\text{atm}}(\text{CO}_2)$	$1.5 \text{ mmol m}^{-3}$	Standard deviation of $C_{\text{atm}}(\text{CO}_2)$
$C(\text{CO}_2)$	$0.8 \text{ mmol m}^{-3}$	Standard deviation of the differences to discrete water samples
$k_w(\text{CO}_2), k_w(\text{O}_2)$	20 %	(Wanninkhof, 2014)
$z_{\text{mix}}$	9 m	Standard deviation for $z_{\text{mix}}$ based on thresholds $\Delta T = 0.1 \text{ }^\circ\text{C}$ (Sprintall and Roemmich, 1999), $0.2 \text{ }^\circ\text{C}$ (Thompson, 1976) and $0.8 \text{ }^\circ\text{C}$ (Kara et al., 2000).
$c(\text{O}_2)$	$2.4 \mu\text{mol kg}^{-1}$	Standard deviation of glider oxygen concentrations for $\sigma_0 > 1028 \text{ kg m}^{-3}$ and latitude $> 64^\circ \text{ N}$

422

### 423 3 Results

424 The uncorrected  $p(\text{CO}_2)$  presented in Figure 8 were analysed up to dive 400 (24 July 2014). For the following  
 425 dives, the  $\text{CO}_2$  optode stopped sampling in the first 150 m (Figure 8d). Instead, the uncorrected temperature  $\theta$ ,  
 426 salinity  $S$ ,  $c(\text{O}_2)$  and  $c_{\text{raw}}(\text{Chl } a)$  were analysed for all the dives (30 October 2014). The raw optode  $c(\text{O}_2)$  data  
 427 was calibrated and drift-corrected and  $c(\text{CO}_2)$  was drift-, lag-corrected and recalibrated, then used to quantify the  
 428 temporal and spatial changes in  $N$  and  $\Phi$  together with the quenching corrected  $c_{\text{raw}}(\text{Chl } a)$  to evaluate net  
 429 community production changes.

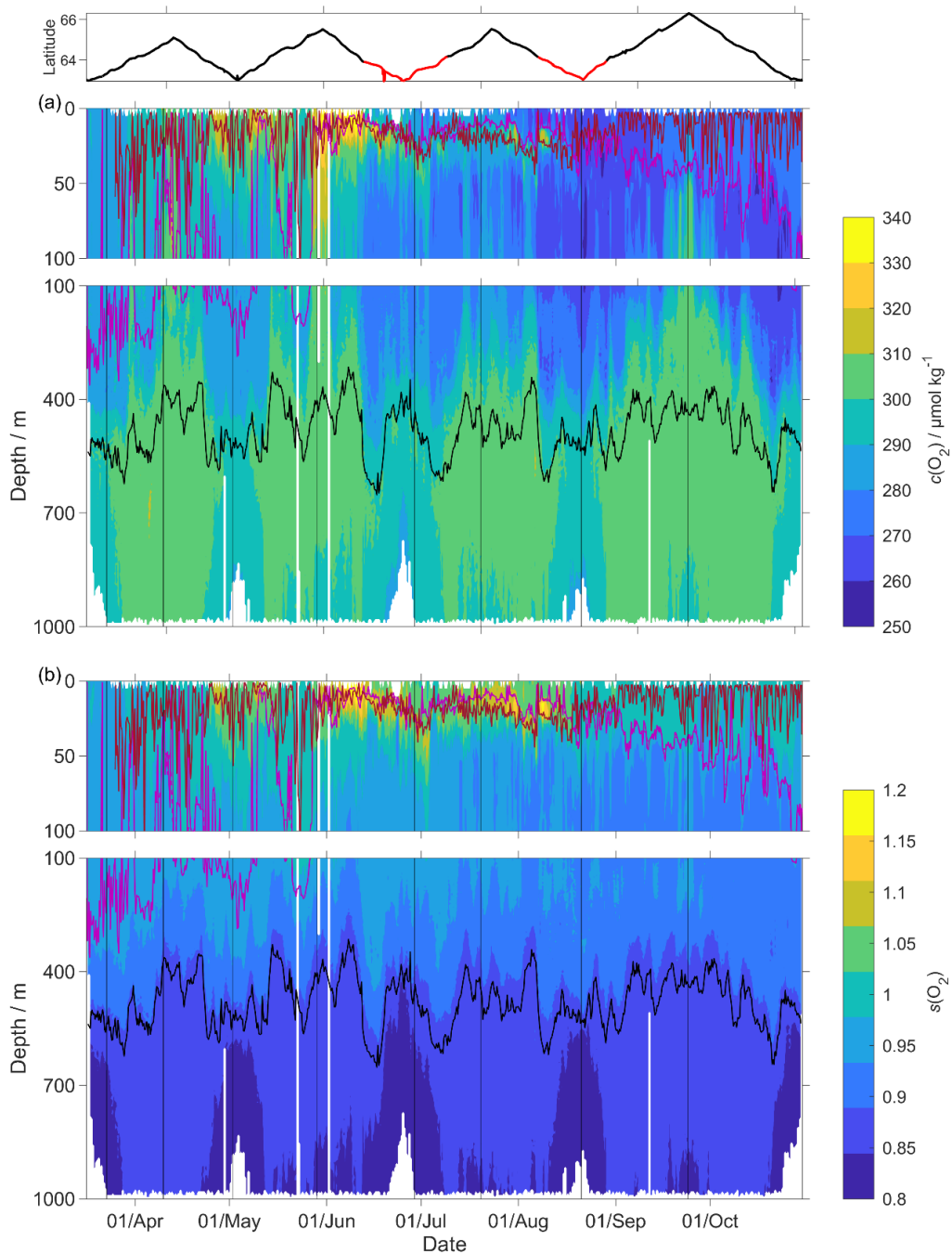




430  
 431 **Figure 8:** Raw glider data for all 703 dives with latitude of the glider trajectory at the top (black: NwAC; red:  
 432 NCC, separated by a  $S$  of 35). a) temperature  $\theta$ , b) salinity  $S$ , c) oxygen concentration  $c_G(\text{O}_2)$ , d) uncorrected  $\text{CO}_2$   
 433 optode output  $p_u(\text{CO}_2)$  and e) chlorophyll  $a$  concentration  $c_{\text{raw}}(\text{Chl } a)$ . The white space means that the sensors did  
 434 not measure any data. The pink line is  $z_{\text{mix}}$  calculated using a threshold criterion of  $\Delta\theta = 0.5 \text{ }^\circ\text{C}$  to the median  $\theta$   
 435 in the top 5 m (Obata et al., 1996; United States. National Environmental Satellite and Information Service,  
 436 Monterey and Levitus, 1997; Foltz et al., 2003). Black dotted line designates  $z_{\text{lim}}$ , used as depth limit to calculate  
 437  $N$ . Black contour lines represent isopycnals.

438 **3.1 O<sub>2</sub> and CO<sub>2</sub> optode calibration**

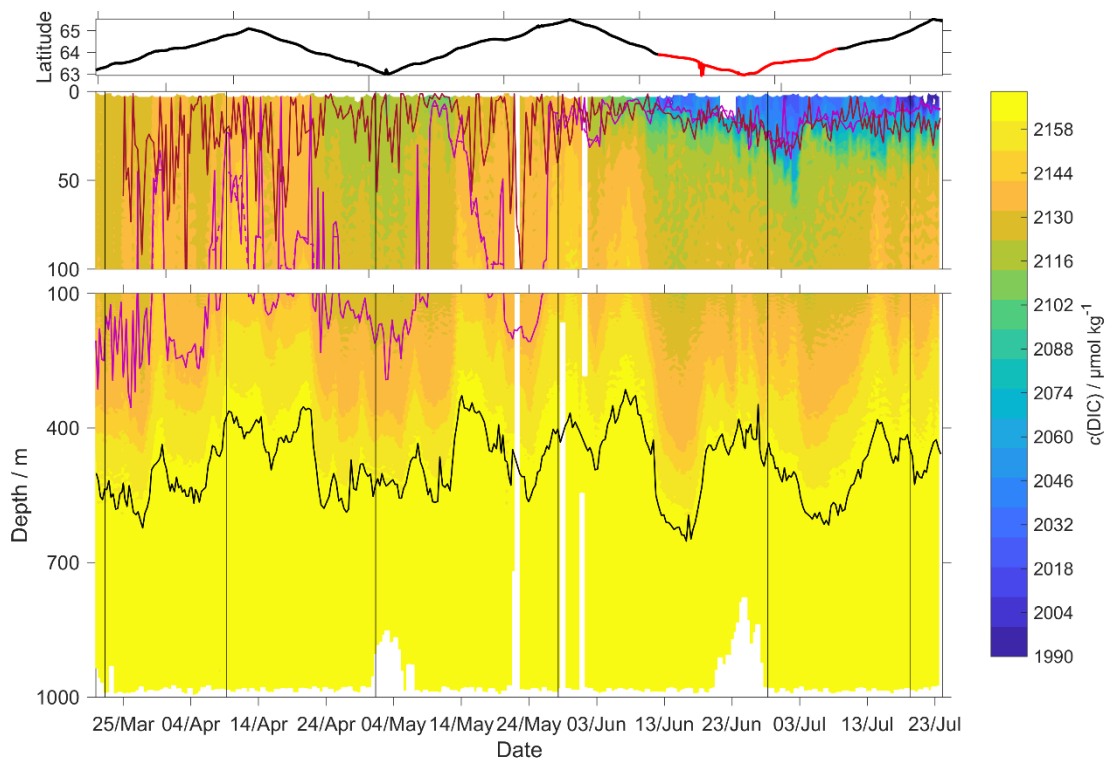
439 The O<sub>2</sub> optode drift caused a continuous and unexpected decrease of the uncorrected  $c_G(\text{O}_2)$  from 290 to 282  
 440  $\mu\text{mol kg}^{-1}$  for  $\sigma_0 > 1028 \text{ kg m}^{-3}$  (Figure 8c). The ratio  $c_C(\text{O}_2)/c_G(\text{O}_2)$  against day of the year used for the drift  
 441 correction had a good correlation with time ( $R^2 = 0.90$ ), showing a continuous increase of  $0.0004 \text{ d}^{-1}$  (Figure 3),  
 442 equivalent to a decrease in the measured glider O<sub>2</sub> concentration of  $0.11 \mu\text{mol kg}^{-1} \text{ d}^{-1}$ . It was possible to apply  
 443 the correction because  $c_C(\text{O}_2)$  had low temporal variability for the chosen potential density  $\sigma_0 > 1028 \text{ kg m}^{-3}$ . The  
 444  $c_C(\text{O}_2)$  values from OWSM and GLODAPv2 had a mean of  $(305 \pm 3) \mu\text{mol kg}^{-1}$ , varying from 294 to  $315 \mu\text{mol}$   
 445  $\text{kg}^{-1}$  (Figure A1). The drift correction reduced the variability of  $c_G(\text{O}_2)$  in the selected potential density range  
 446 from a standard deviation of  $7.3 \mu\text{mol kg}^{-1}$  to a standard deviation of  $2.4 \mu\text{mol kg}^{-1}$  (Figure 9a).  
 447



448  
 449 **Figure 9:** a)  $c(\text{O}_2)$ ; b)  $s(\text{O}_2) = c(\text{O}_2)/c_{\text{sat}}(\text{O}_2)$  with  $z_{\text{DCM}}$  (red line),  $z_{\text{mix}}$  (pink line) 5-point median  $z_{\text{mix}}$  (pink dotted  
 450 line). Black line:  $\sigma_0 = 1028 \text{ kg m}^{-3}$ . Top panel: glider latitude (black: NwAC; red: NCC).

451 Following drift, lag and scale corrections, glider fugacity  $f_G(\text{CO}_2)$  derived from Eq. 2 had a mean difference of  
 452  $(2 \pm 22) \mu\text{atm}$  to the discrete samples ( $n = 55$ ; not shown) and  $c(\text{DIC})$  had a mean difference of  $(3 \pm 11) \mu\text{mol kg}^{-1}$   
 453 (Figure 10).  $p(\text{CO}_2)$  and  $f(\text{CO}_2)$  are almost identical, but  $f(\text{CO}_2)$  takes into account the non-ideal nature of the gas  
 454 phase. The optode was able to capture the temporal and spatial variability showing that NCC had a lower DIC  
 455 concentration than NwAC. Restricting the  $f(\text{CO}_2)$  comparison to the discrete samples in the top 10 m gave a  
 456 mean difference of  $(19 \pm 31) \mu\text{atm}$  ( $n = 6$ ). We also compared glider  $f_G(\text{CO}_2)$  with SOCAT  $f(\text{CO}_2)$  (Bakker et al.,  
 457 2016) data in the region during the deployment (Figure 11). During the whole deployment, there was general  
 458 agreement between  $f_G(\text{CO}_2)$  and  $f_{\text{SOCAT}}(\text{CO}_2)$ .  $f_G(\text{CO}_2)$  varied between 204 and 391  $\mu\text{atm}$  while  $f_{\text{SOCAT}}(\text{CO}_2)$   
 459 varied between 202 and 428  $\mu\text{atm}$  (Figure 11).

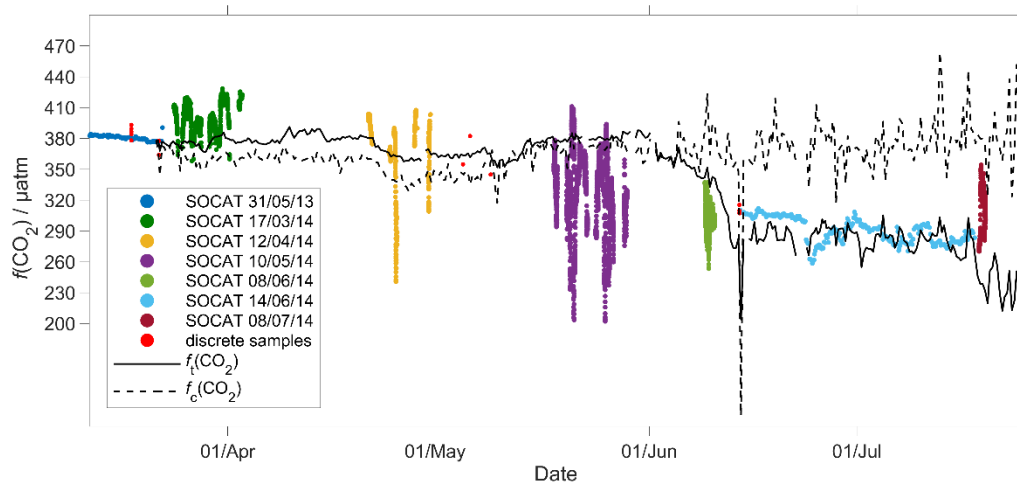
460 Our results are in agreement with Jeansson et al. (2011) who found the surface NCC was the region with the  
 461 lowest  $c(\text{DIC})$  values ( $2083 \mu\text{mol kg}^{-1}$ ) in the Norwegian Sea. This was confirmed during our deployment  
 462 because  $c(\text{DIC})$  was  $(2081 \pm 39) \mu\text{mol kg}^{-1}$  in the NCC region and  $(2146 \pm 27) \mu\text{mol kg}^{-1}$  in the NwAC region  
 463 (Figure 10) and  $c(\text{O}_2)$  was  $> 300 \mu\text{mol kg}^{-1}$  in the NwAC and  $< 280 \mu\text{mol kg}^{-1}$  in the NCC.



464  
 465 **Figure 10:**  $c(\text{DIC})$  contour plot with  $z_{\text{DCM}}$  (red line),  $z_{\text{mix}}$  (pink line) 5-point median  $z_{\text{mix}}$  (pink dotted line). Black  
 466 line:  $\sigma_0 = 1028 \text{ kg m}^{-3}$ . Top panel: glider latitude (black: NwAC; red: NCC).

467

468



469

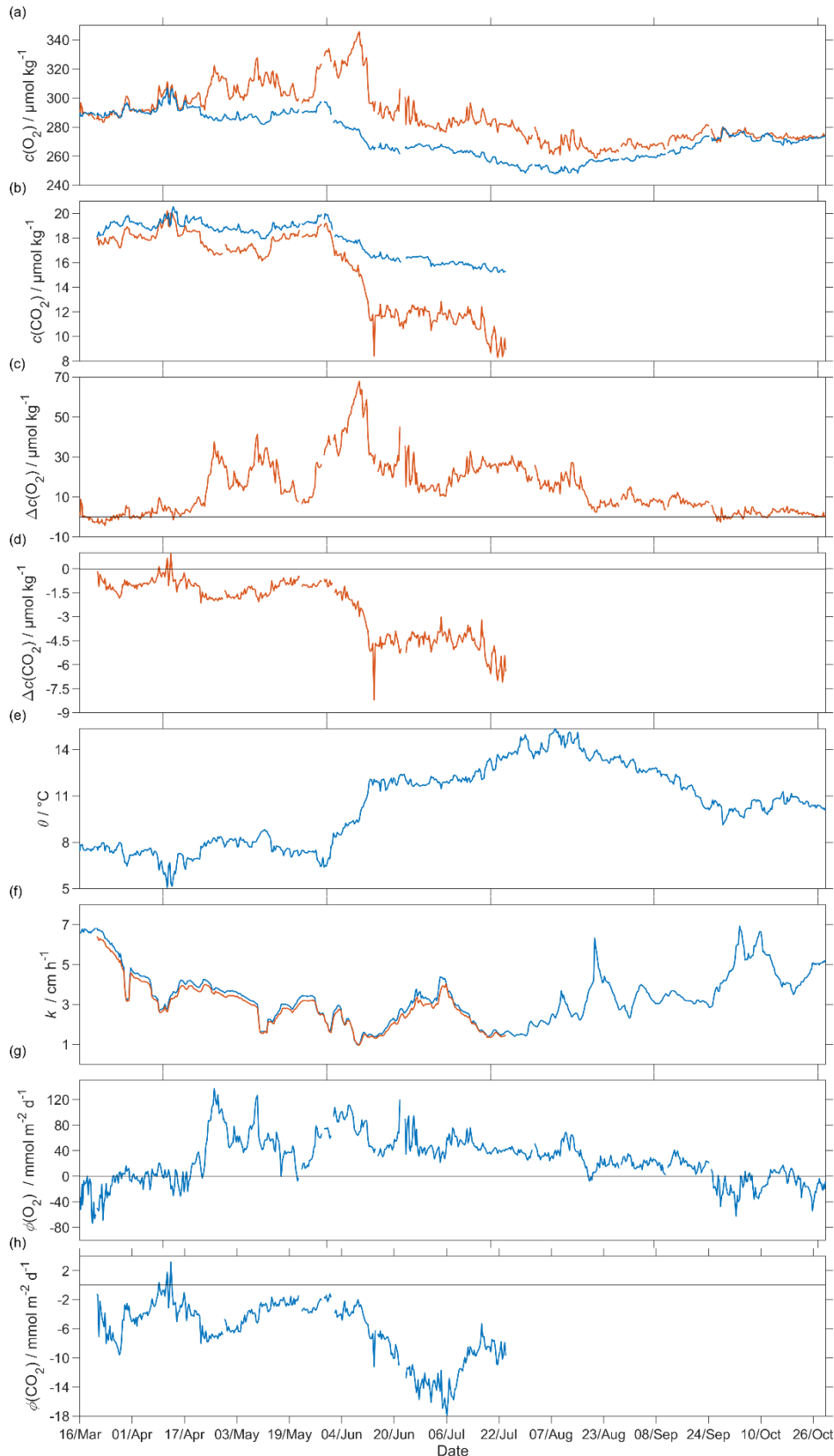
470 **Figure 11:** Comparison between surface  $f(\text{CO}_2)$  from 2014 SOCAT and  $\text{CO}_2$  optode on the glider. Top panel:  
 471 The black lines are the median glider  $f(\text{CO}_2)$  in the top 10 meters, with  $f_c(\text{CO}_2)$  (dotted line) corresponding to  
 472 regression 1 (Figure 6a) and  $f_i(\text{CO}_2)$  (continuous line) to regression 2 (Figure 6a). Discrete samples collected  
 473 during the deployment are shown as red dots, with the other coloured dots representing cruises in the SOCAT  
 474 database (Bakker et al., 2016). Bottom panel: Glider and SOCAT data positions (same colours as in the top  
 475 panel).

476

### 477 3.2 Air-sea exchange

478 The surface water was supersaturated with oxygen all summer (Figure 12). From May, this supersaturation drove  
 479 a continuous  $\text{O}_2$  flux from the sea to the atmosphere. However, the flux varied throughout the deployment having  
 480 a median of  $25 \text{ mmol m}^{-2} \text{ d}^{-1}$  (5<sup>th</sup> centile:  $-31 \text{ mmol m}^{-2} \text{ d}^{-1}$ ; 95<sup>th</sup> centile:  $88 \text{ mmol m}^{-2} \text{ d}^{-1}$ ). Prior to the spring  
 481 period of increased Chl *a* inventory, the supersaturation varied between 0 to  $10 \mu\text{mol kg}^{-1}$ .  $\Phi(\text{O}_2)$  had a median  
 482 of  $-1.4 \text{ mmol m}^{-2} \text{ d}^{-1}$  (5<sup>th</sup> centile:  $-49 \text{ mmol m}^{-2} \text{ d}^{-1}$ ; 95<sup>th</sup> centile:  $23 \text{ mmol m}^{-2} \text{ d}^{-1}$ ). Then, during the spring period  
 483 of increased Chl *a* inventory, the surface concentration increased by over  $35 \mu\text{mol kg}^{-1}$ , causing a peak in  $\Phi(\text{O}_2)$   
 484 of  $140 \text{ mmol m}^{-2} \text{ d}^{-1}$ . A second period of increased Chl *a* inventory was encountered in June and had a larger  
 485  $\Phi(\text{O}_2)$  up to  $118 \text{ mmol m}^{-2} \text{ d}^{-1}$ , driven by supersaturation of  $68 \mu\text{mol kg}^{-1}$ . The fluxes were smaller than during  
 486 spring and were associated by an increase of  $c_{\text{raw}}(\text{Chl } a)$  from  $2.5 \text{ mg m}^{-3}$  to the summer maximum of  $4.0 \text{ mg m}^{-3}$ .  
 487 However, prior to the increased spring Chl *a* inventory,  $\Phi(\text{O}_2)$  showed a few days of influx into seawater caused

488 by a decrease of  $\theta$  from 7.6 °C to 5.9 °C that increased  $C_{\text{sat}}(\text{O}_2)$ . The influx at the beginning of the deployment is  
 489 partly due to the  $\Delta_{\text{bub}}(\text{O}_2)$  correction that resulted in  $[1 + \Delta_{\text{bub}}(\text{O}_2)]c_{\text{sat}}(\text{O}_2) > c(\text{O}_2)$  for  $U > 10 \text{ m s}^{-1}$ . In August the  
 490 surface supersaturation decreased to  $2.3 \mu\text{mol kg}^{-1}$  and  $\Phi(\text{O}_2)$  decreased to a monthly minimum of  $-7.6 \text{ mmol m}^{-2} \text{ d}^{-1}$   
 491  $^2 \text{ d}^{-1}$ . In the second half of September the surface water became undersaturated by  $-2.6 \mu\text{mol kg}^{-1}$ , causing  $\text{O}_2$   
 492 uptake with a median flux of  $-13 \text{ mmol m}^{-2} \text{ d}^{-1}$  (5<sup>th</sup> centile:  $-39 \text{ mmol m}^{-2} \text{ d}^{-1}$ ; 95<sup>th</sup> centile:  $10 \text{ mmol m}^{-2} \text{ d}^{-1}$ ).



494 **Figure 12:** Air-sea flux of O<sub>2</sub> and CO<sub>2</sub> during spring and summer for CO<sub>2</sub> and during spring, summer and  
 495 autumn for O<sub>2</sub>, a)  $c_{\text{sat}}(\text{O}_2)$  in blue and  $c(\text{O}_2)$  in red, b)  $c_{\text{sat}}(\text{CO}_2)$  in blue and  $c(\text{CO}_2)$  in red, c)  $\Delta c(\text{O}_2) = c(\text{O}_2) -$   
 496  $c_{\text{sat}}(\text{O}_2)$ , d)  $\Delta c(\text{CO}_2) = c(\text{CO}_2) - c_{\text{sat}}(\text{CO}_2)$ , e) sea surface temperature, f)  $k_w(\text{O}_2)$  in blue and  $k_w(\text{CO}_2)$  in red  
 497 normalised back to 50 days (Reuer et al., 2007), g) oxygen air-sea flux  $\Phi(\text{O}_2)$  and h) CO<sub>2</sub> air-sea flux  $\Phi(\text{CO}_2)$ .  
 498 The flux from sea to air is positive while that from air to sea is negative.

499

500 The CO<sub>2</sub> flux from March to July was always from the air to the sea (Figure 12), with a median of  $-5.2 \text{ mmol m}^{-2}$   
 501  $\text{d}^{-1}$  (5<sup>th</sup> centile:  $-14 \text{ mmol m}^{-2} \text{ d}^{-1}$ ; 95<sup>th</sup> centile:  $-1.5 \text{ mmol m}^{-2} \text{ d}^{-1}$ ). An opposite flux direction is expected for  
 502  $\Phi(\text{O}_2)$  and  $\Phi(\text{CO}_2)$  during the productive season when net community production is the main driver of  
 503 concentration changes. After the summer period of increased Chl *a* inventory, the flux had a median of  $-11 \text{ mmol}$   
 504  $\text{m}^{-2} \text{ d}^{-1}$  (5<sup>th</sup> centile:  $-16 \text{ mmol m}^{-2} \text{ d}^{-1}$ ; 95<sup>th</sup> centile:  $-6.8 \text{ mmol m}^{-2} \text{ d}^{-1}$ ), in agreement with previous studies that  
 505 classified the Norwegian Sea as a CO<sub>2</sub> sink (Takahashi et al., 2002; Skjelvan et al., 2005).  $\Phi(\text{CO}_2)$  for the  
 506 discrete samples from 18 March to 14 June ( $n = 13$ ) varied from 0.1 to  $-13 \text{ mmol m}^{-2} \text{ d}^{-1}$ .

507

### 508 3.3 $N(\text{O}_2)$

509 To capture the entire euphotic zone, we calculated  $N(\text{O}_2)$  and  $N(\text{DIC})$  using an integration depth of  $z_{\text{lim}} = 45 \text{ m}$   
 510 because the mean deep chlorophyll maximum (DCM) depth was  $z_{\text{DCM}} = (20 \pm 18 \text{ m})$  (Figure 9). For comparison,  
 511 the mixed layer depth was deeper, varied more strongly and had a mean value of  $z_{\text{mix}} = (68 \pm 78 \text{ m})$ , using a  
 512 threshold criterion of  $\Delta\theta = 0.5 \text{ }^\circ\text{C}$  to the median  $\theta$  value in the top 5 m of the glider profile (Obata et al., 1996;  
 513 United States. National Environmental Satellite and Information Service, Monterey and Levitus, 1997; Foltz et  
 514 al., 2003).

515 The two  $N$  values were calculated as the difference in inventory changes between two transects when the glider  
 516 moved in the same direction.

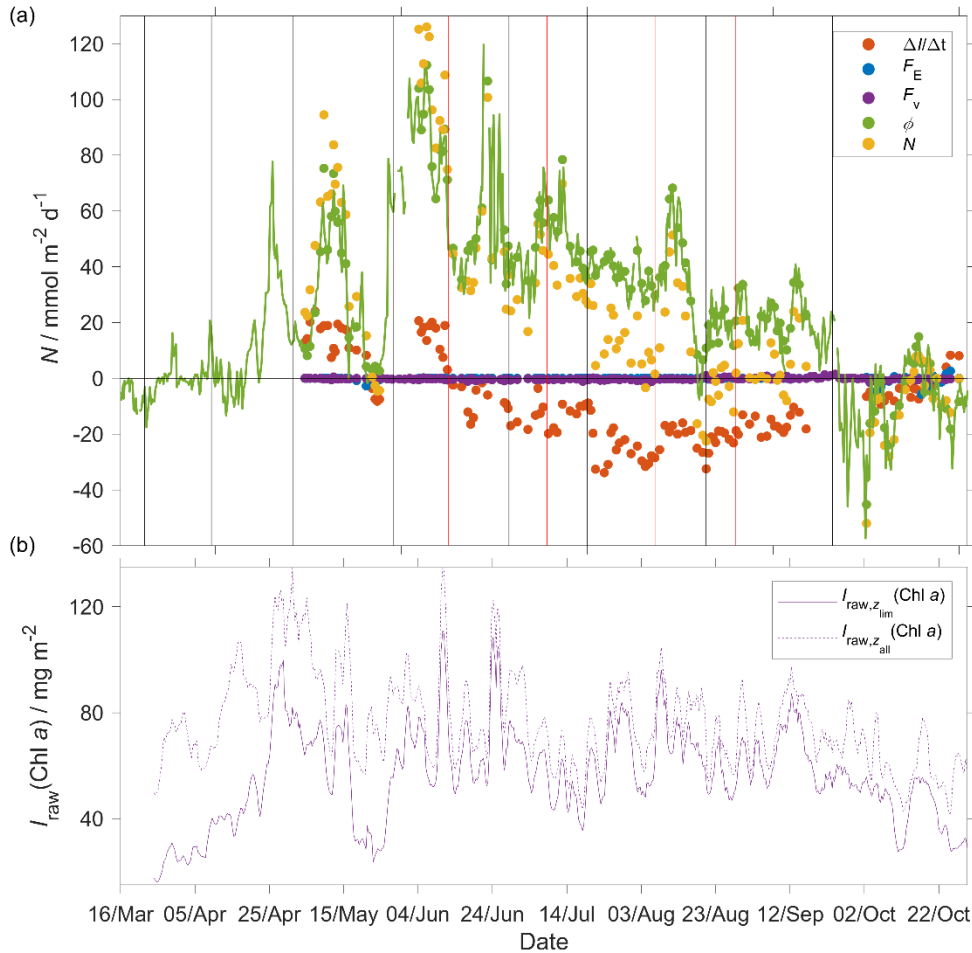
517 During the deployment, we sampled two periods of increased Chl *a* inventory, the first one in May and a second  
 518 one in June. The chlorophyll *a* inventory ( $I_{\text{raw},z_{\text{lim}}}(\text{Chl } a)$ ) was calculated integrating  $c_{\text{raw}}(\text{Chl } a)$  to  $z_{\text{lim}}$ . To  
 519 remove outliers we used a five-point moving mean of  $I_{\text{raw},z_{\text{lim}}}(\text{Chl } a)$ .

520 The  $N(\text{O}_2)$  changes were dominated by  $\Phi(\text{O}_2)$  that had an absolute median of  $34 \text{ mmol m}^{-2} \text{ d}^{-1}$  (5<sup>th</sup> centile:  $4.3$   
 521  $\text{mmol m}^{-2} \text{ d}^{-1}$ ; 95<sup>th</sup> centile:  $86 \text{ mmol m}^{-2} \text{ d}^{-1}$ ), followed by  $I(\text{O}_2)$  that had a median of  $15 \text{ mmol m}^{-2} \text{ d}^{-1}$  (5<sup>th</sup> centile:  
 522  $2.3 \text{ mmol m}^{-2} \text{ d}^{-1}$ ; 95<sup>th</sup> centile:  $29 \text{ mmol m}^{-2} \text{ d}^{-1}$ ),  $F_v(\text{O}_2)$  that had an absolute median of  $0.3 \text{ mmol m}^{-2} \text{ d}^{-1}$  (5<sup>th</sup>  
 523 centile:  $0 \text{ mmol m}^{-2} \text{ d}^{-1}$ ; 95<sup>th</sup> centile:  $1.0 \text{ mmol m}^{-2} \text{ d}^{-1}$ ) and  $E(\text{O}_2)$  that had a median of  $0 \text{ mmol m}^{-2} \text{ d}^{-1}$  (5<sup>th</sup> centile:  
 524  $-1.2 \text{ mmol m}^{-2} \text{ d}^{-1}$ ; 95<sup>th</sup> centile:  $0 \text{ mmol m}^{-2} \text{ d}^{-1}$ ).

525 At the beginning of May,  $I_{\text{raw},z_{\text{lim}}}(\text{Chl } a)$  increased to  $97 \text{ mg m}^{-2}$  and  $N(\text{O}_2) = (95 \pm 16) \text{ mmol m}^{-2} \text{ d}^{-1}$ . After this  
 526 period,  $I_{\text{raw},z_{\text{lim}}}(\text{Chl } a)$  decreased to  $49 \text{ mg m}^{-2}$  and  $N(\text{O}_2) = (-4.6 \pm 1.6) \text{ mmol m}^{-2} \text{ d}^{-1}$ . During the summer  
 527  $I_{\text{raw},z_{\text{lim}}}(\text{Chl } a)$  increased to  $110 \text{ mg m}^{-2}$ , which caused a sharp increase of  $N(\text{O}_2)$  to  $(126 \pm 25) \text{ mmol m}^{-2} \text{ d}^{-1}$ .  
 528  $I_{\text{raw},z_{\text{lim}}}(\text{Chl } a)$  remained higher than  $50 \text{ mg m}^{-2}$  until the end of June when  $N(\text{O}_2)$  was  $(31 \pm 9) \text{ mmol m}^{-2} \text{ d}^{-1}$ . The  
 529 passage of the glider from NwAC to NCC accompanied by a drop of surface  $c(\text{O}_2)$  from  $330$  to  $280 \text{ } \mu\text{mol kg}^{-1}$   
 530 (Figure 9) that resulted in lower  $\Phi(\text{O}_2)$  and  $N(\text{O}_2)$  values (Figure 13). At the same time  $I_{\text{raw},z_{\text{lim}}}(\text{Chl } a)$

531 decreased to  $35 \text{ mg m}^{-2}$  showing that the decrease of  $N(\text{O}_2)$  depended on the passage to NCC and a decrease of  
 532 biological production. After the beginning of August,  $I_{\text{raw},z_{\text{lim}}}(\text{Chl } a)$  decreased to  $49 \text{ mg m}^{-2}$  and  $N(\text{O}_2)$  turned  
 533 negative with a minimum of  $(-23 \pm 25) \text{ mmol m}^{-2} \text{ d}^{-1}$ . In October during the last glider transect  $I_{\text{raw},z_{\text{lim}}}(\text{Chl } a)$   
 534 continued decreasing to  $27 \text{ mg m}^{-2}$  leading to the minimum  $N(\text{O}_2)$  of  $(-52 \pm 11) \text{ mmol m}^{-2} \text{ d}^{-1}$ .

535 Integrating  $N(\text{O}_2)$  from March to October gives a flux of  $4.9 \text{ mol m}^{-2} \text{ a}^{-1}$  (Table 3; discussed in section 4.2).



536 **Figure 13:** a) Components of the  $N(\text{O}_2)$  calculation:  $\Delta I(\text{O}_2)/\Delta t$  (red),  $E(\text{O}_2)$  (blue),  $F_v(\text{O}_2)$  (violet),  $\Phi(\text{O}_2)$  (green)  
 537 with  $k_w(\text{O}_2)$  weighted over 50 days,  $N(\text{O}_2)$  (yellow). b) Chl *a* inventory in the top 45 m,  $I_{\text{raw},z_{\text{lim}}}(\text{Chl } a)$  (violet).  
 538 Chl *a* inventory for the whole water column,  $I_{\text{raw},z_{\text{all}}}(\text{Chl } a)$  (violet dotted line). The black vertical lines  
 539 represent each glider transect. Between the two vertical red lines, the glider was in the NCC region.  
 540  
 541

### 542 3.4 $N(\text{DIC})$

543 In the case of  $N(\text{DIC})$  the main drivers were the inventory changes with an absolute median of  $29 \text{ mmol m}^{-2} \text{ d}^{-1}$   
 544 (5<sup>th</sup> centile:  $1.3 \text{ mmol m}^{-2} \text{ d}^{-1}$ ; 95<sup>th</sup> centile:  $57 \text{ mmol m}^{-2} \text{ d}^{-1}$ ), followed by  $\Phi(\text{CO}_2)$  that had an absolute median of  
 545  $7.0 \text{ mmol m}^{-2} \text{ d}^{-1}$  (5<sup>th</sup> centile:  $0.8 \text{ mmol m}^{-2} \text{ d}^{-1}$ ; 95<sup>th</sup> centile:  $15 \text{ mmol m}^{-2} \text{ d}^{-1}$ ),  $F_v(\text{DIC})$  that had an absolute  
 546 median of  $0.2 \text{ mmol m}^{-2} \text{ d}^{-1}$  (5<sup>th</sup> centile:  $0 \text{ mmol m}^{-2} \text{ d}^{-1}$ ; 95<sup>th</sup> centile:  $1.3 \text{ mmol m}^{-2} \text{ d}^{-1}$ ) and  $E(\text{DIC})$  had a median  
 547 of  $0 \text{ mmol m}^{-2} \text{ d}^{-1}$  (5<sup>th</sup> centile:  $0 \text{ mmol m}^{-2} \text{ d}^{-1}$ ; 95<sup>th</sup> centile:  $3.4 \text{ mmol m}^{-2} \text{ d}^{-1}$ ). During the period of increased Chl  
 548 *a* inventory  $N(\text{DIC})$  was  $(21 \pm 4.5) \text{ mmol m}^{-2} \text{ d}^{-1}$ . Later  $I_{\text{raw},z_{\text{lim}}}(\text{Chl } a)$  decreased to  $30 \text{ mg m}^{-2}$  driving  $N(\text{DIC})$  to  
 549 negative values with a minimum of  $(-2.7 \pm 5.0) \text{ mmol m}^{-2} \text{ d}^{-1}$ . In the next transect, the glider measured the

550 maximum  $I_{\text{raw}, z_{\text{lim}}}(\text{Chl } a)$  of  $111 \text{ mg m}^{-2}$  that increased  $N(\text{DIC})$  to  $(85 \pm 4.5) \text{ mmol m}^{-2} \text{ d}^{-1}$ . This maximum was  
 551 reached during a transect when the glider moved in NCC that had a  $c(\text{DIC})$  of  $2080 \text{ } \mu\text{mol kg}^{-1}$  at the surface  
 552 compared with the  $2150 \text{ } \mu\text{mol kg}^{-1}$  in NwAC and drove a continuous positive  $N(\text{DIC})$  that had a minimum of  
 553  $(36 \pm 7.4) \text{ mmol m}^{-2} \text{ d}^{-1}$  (Figure 14).

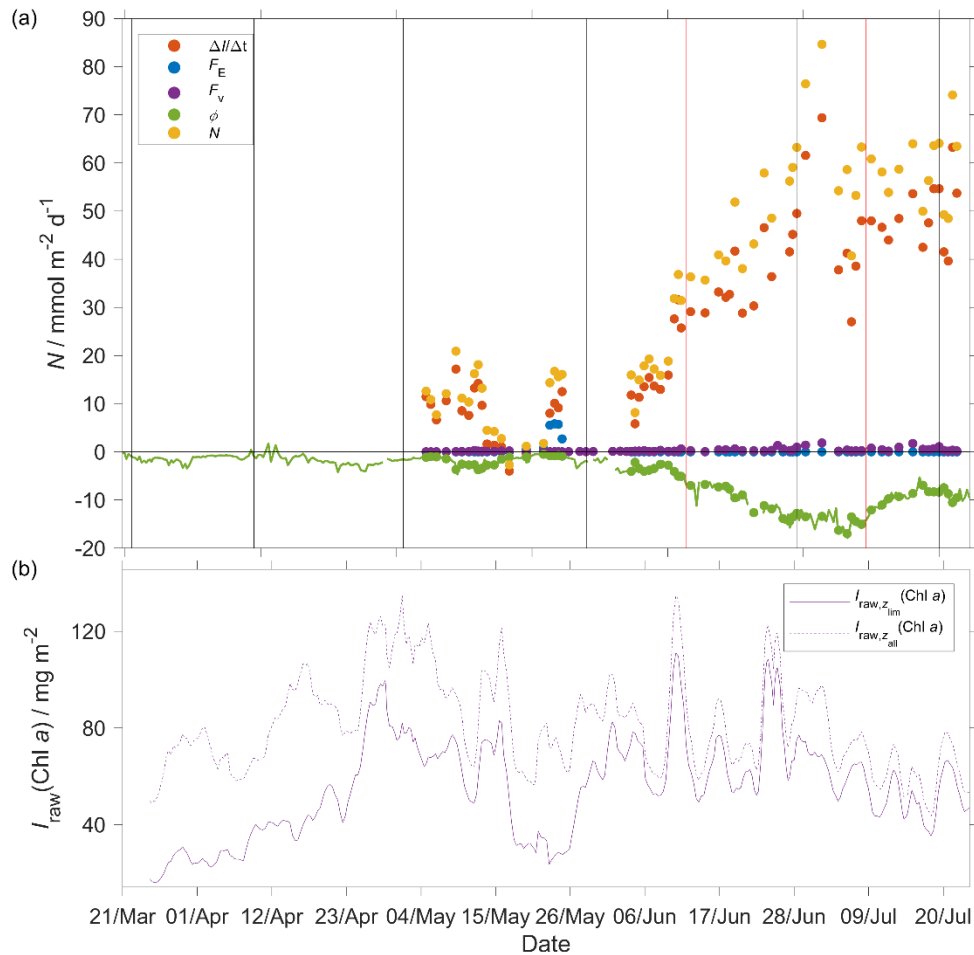
554 Integrating  $N(\text{DIC})$  from March to July gives a flux of  $3.3 \text{ mol m}^{-2} \text{ a}^{-1}$  (Table 3; discussed in section 4.2).

555  
 556 **Table 3.** Net community production ( $N$ ) estimates in the Norwegian Sea (with integration depth  $z_{\text{lim}}$ ). Falck and  
 557 Anderson (2005) used year-round data from 1960 to 2000 between  $62$  and  $70^\circ \text{ N}$  and from 1991 to 1994 at  
 558 OWSM. Skjelvan et al. (2001) used year-round data from 1957 to 1970 and from 1991 to 1998 between  $67.5^\circ \text{ N}$   
 559  $9^\circ \text{ E}$  and  $71.5^\circ \text{ N } 1^\circ \text{ E}$  and along  $74.5^\circ \text{ N}$  from  $7$  to  $15^\circ \text{ E}$ . Kivimäe (2007) used year-round data from 1955 to  
 560 2005 and Falck and Gade (1999) used year-round data from 1955 to 1988 in all of the Norwegian Sea. While the  
 561 previous studies report annual  $N$  estimates, the present study derives  $N(\text{O}_2)$  between March and October and  
 562  $N(\text{DIC})$  between March and July.

563

Study	$N(\text{DIC}) /$ $\text{mol m}^{-2}$ $\text{a}^{-1}$	$N(\text{O}_2) /$ $\text{mol m}^{-2}$ $\text{a}^{-1}$	$N(\text{O}_2) /$ $N(\text{DIC})$	$z_{\text{lim}} / \text{m}$	Variables used to derive $N$
(Falck and Anderson, 2005), annual	3.4	—	—	100	$c(\text{NO}_3^-)$ , $c(\text{PO}_4^{3-})$ , $c(\text{DIC})$
(Skjelvan et al., 2001), annual	—	2.6	—	300	$c(\text{O}_2)$ , $c(\text{PO}_4^{3-})$
(Kivimäe, 2007), annual	—	11 (4.7 to 18.3)	—	$z_{\text{mix}}$ until 100 m	$c(\text{O}_2)$
(Falck and Gade, 1999), annual	—	3.9	—	30	$c(\text{O}_2)$
This study, March to July	3.1	4.1	1.3	30	$c(\text{O}_2)$ , $c(\text{DIC})$
This study, March to July	3.3	4.2	1.3	45	$c(\text{O}_2)$ , $c(\text{DIC})$
This study, March to July	3.3	3.7	1.1	100	$c(\text{O}_2)$ , $c(\text{DIC})$
This study, March to October	—	5.0	—	—	—
This study, March to October	—	4.9	—	—	—
This study, March to October	—	3.6	—	—	—





564  
565  
566  
567  
568  
569  
570

**Figure 14:** a) Components of the  $N(\text{DIC})$  calculation:  $\Delta I(\text{DIC})/\Delta t$  (red),  $E(\text{DIC})$  (blue),  $F_v(\text{CO}_2)$  (violet),  $\Phi(\text{CO}_2)$  (green) with  $k_w(\text{CO}_2)$  weighted over 50 days,  $N(\text{DIC})$  (yellow). b) Chl *a* inventory in the top 45 m,  $I_{\text{raw},z_{\text{lim}}}(\text{Chl } a)$  (violet). Chl *a* inventory for the whole water column,  $I_{\text{raw},z_{\text{all}}}(\text{Chl } a)$  (violet dotted line). The black vertical lines represent each glider transect. Between the two vertical red lines, the glider was in the NCC region.

## 571 4 Discussion

### 572 4.1 Sensor performance

573 This study presents data from the first glider deployment with a  $\text{CO}_2$  optode. The initial uncalibrated  $p_{\text{a}}(\text{CO}_2)$   
574 measured by the  $\text{CO}_2$  optode had a median of 604  $\mu\text{atm}$  (5<sup>th</sup> centile: 566  $\mu\text{atm}$ ; 95<sup>th</sup> centile: 768  $\mu\text{atm}$ ), whereas  
575 the  $p(\text{CO}_2)$  of discrete samples varied from 302 to 421  $\mu\text{atm}$ .

576 We applied corrections for drift (using deep-water samples as a reference point), sensor lag and calibrated the  
577  $\text{CO}_2$  optode against co-located discrete samples throughout the water column.

578 Atamanchuk (2014) reported that the sensor was affected by a lag that varied from 45 to 264 s depending on  
579 temperature. These values were determined in an actively stirred beaker. However, in this study the sensor was  
580 mounted on a glider and was not actively pumped, which increased the response time to 23 min (25<sup>th</sup> quartile: 18  
581 min; 75<sup>th</sup> quartile: 30 min). Also, the optode was affected by a continuous drift from 637 to 5500  $\mu\text{atm}$  that is  
582 larger than the drift found by Atamanchuk et al. (2015a) that increased by 75  $\mu\text{atm}$  after 7 months.

583 In this study, the drift- and lag-corrected sensor output showed a better correlation with the CO<sub>2</sub> concentration  
584  $c(\text{CO}_2)$  than with  $p(\text{CO}_2)$ . The latter two quantities are related to each other by the solubility that varies with  $\theta$   
585 and  $S$  (Weiss, 1974) (Eq. 2). The better correlation with  $c(\text{CO}_2)$  was probably related due to an inadequate  
586 temperature-parameterisation of the sensor calibration function. Including temperature and temperature squared  
587 in the calibration gave a better fit for both  $c(\text{CO}_2)$  than with  $p(\text{CO}_2)$ , but overall still a lower calibration residual  
588 for the former. The sensor output depends on the changes in pH that are directly related to the changes of  $c(\text{CO}_2)$   
589 in the membrane and – indirectly –  $p(\text{CO}_2)$ , via Henry's Law. The calibration is supposed to correct for the  
590 temperature-dependence of the sensor output (Atamanchuk et al., 2014). So the fact, that the sensor output  
591 correlated better with  $c(\text{CO}_2)$  than  $p(\text{CO}_2)$  is perhaps due to a fortuitous cancellation of an inadequate  
592 temperature-parameterisation and the Henry's Law relationship between  $c(\text{CO}_2)$  than  $p(\text{CO}_2)$ .

593 The calibrated optode output captured the  $c(\text{DIC})$  changes in space and time with a standard deviation of 11  
594  $\mu\text{mol kg}^{-1}$  compared with the discrete samples.  $c(\text{DIC})$  decreased from 2130  $\mu\text{mol kg}^{-1}$  to 2000  $\mu\text{mol kg}^{-1}$  and  
595 increased with depth to 2170  $\mu\text{mol kg}^{-1}$ . This shows the potential of the sensor for future studies that aim to  
596 analyse the carbon cycle using a high-resolution dataset.

597 The optode-derived CO<sub>2</sub> fugacity  $f_G(\text{CO}_2)$  had a mean bias of  $(1.8 \pm 22)$   $\mu\text{atm}$  compared with the discrete samples.  
598 These values are comparable with a previous study when the CO<sub>2</sub> optode was tested for 65 days on a wave-  
599 powered Profiling cRAWLER (PRAWLER) from 3 to 80 m (Chu et al., 2020), which had an uncertainty  
600 between 35 and 72  $\mu\text{atm}$ . The PRAWLER optode was affected by a continuous drift of 5.5  $\mu\text{atm d}^{-1}$  corrected  
601 using a regional empirical algorithm that uses  $c(\text{O}_2)$ ,  $\theta$ ,  $S$  and  $\sigma_\theta$  to estimate  $A_T$  and  $c(\text{DIC})$ .

#### 602 4.2 Norwegian Sea net community production

603 Increases in  $N(\text{O}_2)$  and  $N(\text{DIC})$  were associated with increases in depth-integrated  $c_{\text{raw}}(\text{Chl } a)$ , designated as  
604 periods of increased Chl  $a$  inventory  $I_{\text{raw}}(\text{Chl } a)$ , at the beginning of May and in June. During May,  $I_{\text{raw}}(\text{Chl } a)$   
605 reached 135  $\text{mg m}^{-2}$ . In June,  $I_{\text{raw}}(\text{Chl } a)$  reached again 135  $\text{mg m}^{-2}$ . Between these two periods,  $N(\text{DIC})$  briefly  
606 turned negative, indicating remineralisation of the high Chl  $a$  inventory material during this period. The period  
607 of increased Chl  $a$  inventory coincided with a surface temperature increase from 7 °C to 11 °C and shoaling of  
608 the mixed layer from 200 m to 20 m.  $c(\text{O}_2)$  reached a summer maximum of 340  $\mu\text{mol kg}^{-1}$  and  $c(\text{DIC})$  decreased  
609 to a summer minimum of 1990  $\mu\text{mol kg}^{-1}$ . In both cases, the main components of the  $N$  changes were the  
610 inventory and air-sea flux, while the smallest driver was the entrainment. Also, the glider sampled two different  
611 water masses characterised by different  $c(\text{DIC})$  and  $c(\text{O}_2)$ . This might be the cause of the smaller values  $N(\text{O}_2)$   
612 and higher values  $N(\text{DIC})$  in June and July in NCC compared to NwAC (Figure 13 and 14). Another explanation  
613 might be a consumption of O<sub>2</sub> due to remineralisation and a delay in the response of the  $c(\text{DIC})$  that was lowered  
614 during the two blooms. A fully functional CO<sub>2</sub> optode in the second part of the deployment would have helped to  
615 uncover the cause of the higher  $N(\text{DIC})$  than of  $N(\text{O}_2)$ .

616 Table 3 shows estimates of net community production ( $N$ ) in the Norwegian Sea. All other studies used ships to  
617 gather observations. The estimated  $N$  in of the four other studies varied from 2.6 to 11.1  $\text{mol m}^{-2} \text{a}^{-1}$  for  $N(\text{O}_2)$   
618 and was 3.4 for  $N(\text{DIC})$ . In our glider study, we obtained between March and July  $N(\text{DIC})$  of 3.3  $\text{mol m}^{-2} \text{a}^{-1}$  and  
619 a  $N(\text{O}_2)$  of 4.2  $\text{mol m}^{-2} \text{a}^{-1}$ , in agreement with these studies. The ratio of  $N(\text{O}_2)$  and  $N(\text{DIC})$  for an integration  
620 depth of 45 m gave a photosynthetic quotient (PQ) of 1.3, in agreement with the Redfield ratio of  $1.45 \pm 0.15$   
621 (Redfield, 1963; Anderson, 1995; Anderson and Sarmiento, 1994; Laws, 1991). The  $N(\text{O}_2)$  estimate is influenced

622 primarily by the air-sea exchange flux  $\Phi(\text{O}_2)$  (median:  $34 \text{ mmol m}^{-2} \text{ d}^{-1}$ ), followed by the inventory change (15  
623  $\text{mmol m}^{-2} \text{ d}^{-1}$ ). In contrast,  $N(\text{DIC})$  is dominated by the inventory change ( $-29 \text{ mmol m}^{-2} \text{ d}^{-1}$ ), followed by  
624  $\Phi(\text{CO}_2)$  ( $-7.0 \text{ mmol m}^{-2} \text{ d}^{-1}$ ). This reflects the slower gas-exchange time constant of  $\text{CO}_2$  compared with  $\text{O}_2$ , due  
625 to DIC buffering. To compare our results with previous studies we also used  $z_{\text{lim}} = 30 \text{ m}$  (Falck and Gade, 1999)  
626 and  $100 \text{ m}$  (Falck and Anderson, 2005; Kivimäe, 2007). The calculated  $N(\text{DIC}; 30 \text{ m})$  was  $3.1 \text{ mol m}^{-2} \text{ a}^{-1}$ ,  
627  $N(\text{DIC}; 100 \text{ m})$  was  $3.4 \text{ mol m}^{-2} \text{ a}^{-1}$ ,  $N(\text{O}_2; 30 \text{ m})$  was  $4.1 \text{ mol m}^{-2} \text{ a}^{-1}$  and  $N(\text{O}_2; 100 \text{ m})$  was  $3.7 \text{ mol m}^{-2} \text{ a}^{-1}$ . The  
628  $N(\text{DIC}; 100 \text{ m})$  value is in agreement with the value of  $3.4 \text{ mol m}^{-2} \text{ a}^{-1}$  given by Falck and Anderson (2005).  
629 However, the latter estimate was for the entire year, whereas our estimate only covers the months from March to  
630 July.  $N(\text{O}_2)$  was similar for  $z_{\text{lim}} = 30 \text{ m}$  and  $45 \text{ m}$ , but lower for  $z_{\text{lim}} = 100 \text{ m}$  because of  $\text{O}_2$  consumption during  
631 organic matter remineralisation below the euphotic zone. The PQ value at  $30 \text{ m}$  was  $1.3$  and at  $100 \text{ m}$  decreased to  
632  $1.1$ . Extending  $N(\text{O}_2)$  to October increased  $N(\text{O}_2; 30 \text{ m})$  and  $N(\text{O}_2; 45 \text{ m})$  to  $5.0$  and  $4.9 \text{ mol m}^{-2} \text{ a}^{-1}$ , respectively.  
633 Instead,  $N(\text{O}_2; 100 \text{ m})$  decreased to  $3.6 \text{ mol m}^{-2} \text{ a}^{-1}$ , confirming the consumption of  $\text{O}_2$  below the euphotic zone.  
634 The calculated  $N(\text{O}_2)$  until October was in agreement with the previous studies that varied between  $2.6$  and  $11$   
635  $\text{mol m}^{-2} \text{ a}^{-1}$ .

636 Some of the previous  $N(\text{DIC})$  estimates derived  $c(\text{DIC})$  from other variables such as  $c(\text{O}_2)$ ,  $c(\text{PO}_4^{3-})$ ,  $c(\text{NO}_3^-)$ ,  
637 assuming Redfield ratios P:N:C:O<sub>2</sub> 1:16:106:-138 (Redfield, 1963). During photosynthesis  $c(\text{PO}_4^{3-})$  and  $c(\text{NO}_3^-)$   
638 are taken up by phytoplankton to form organic matter and are released again after remineralisation of the organic  
639 matter giving an indication of NCP changes. Our  $N(\text{DIC})$  estimate was  $3.3 \text{ mol m}^{-2} \text{ a}^{-1}$  and is similar to  $3.4 \text{ mol}$   
640  $\text{m}^{-2} \text{ a}^{-1}$  estimated by Falck and Anderson (2005) who used  $c(\text{DIC})$  samples directly. The carbon/nutrient ratios  
641 vary between water masses and during photosynthesis (Thomas et al., 1999; Copin-Montégut, 2000; Osterroht  
642 and Thomas, 2000; Körtzinger et al., 2001).

643 The difference of the annual  $N(\text{O}_2)$  and  $N(\text{DIC})$  with the previous studies can also be caused by the yearly  
644 variability of  $N$  in the Norwegian Sea. In fact, Kivimäe (2007) saw an annual variability of  $N(\text{O}_2)$  from 1955 to  
645 2005 between  $4.7 \text{ mol m}^{-2} \text{ a}^{-1}$  and  $18.3 \text{ mol m}^{-2} \text{ a}^{-1}$ . In order to understand what is causing these interannual  
646 changes, it is important capture inventory and air-sea changes. Also, this study showed that the Norwegian Sea  
647 spring, summer and autumn  $N$  is strongly affected by time of sampling. For that reason,  $N$  estimated from low-  
648 resolution datasets make the result strongly dependant on the time of sampling. To quantify this interannual  
649 variability in  $N$ , more high-resolution studies are needed.

## 650 **5 Conclusions**

651 To the best of our knowledge, this study represents the first glider deployment of a  $\text{CO}_2$  optode. The  $\text{CO}_2$  optode  
652 together with a  $\text{O}_2$  optode shows the potential of using these sensors on autonomous observing platforms like  
653 Seagliders to quantify the interactions between biogeochemical processes and the marine carbonate system at  
654 high spatiotemporal resolution. The deployment helped to uncover NCP and air-sea flux variability over a period  
655 of 8 months.

656 Despite all the problems (drift, lag and poor calibration), the  $\text{CO}_2$  optode data could be used to quantify  
657 dissolved inorganic carbon concentration variations. The temporal resolution sampling resolution was  $106 \text{ s}$  in  
658 the top  $100 \text{ m}$  (increasing to  $381 \text{ s}$  from  $500$  to  $1000 \text{ m}$ ). This could be improved to less than  $10 \text{ s}$ , but this would  
659 reduce the length of the deployment due to the limited glider battery capacity. With better calibration and  
660 stability improvements, the  $\text{CO}_2$  optode could be routinely used to measure the carbonate system on gliders,

661 floats and surface vehicles. Glider deployments up to 8 months are possible thanks to the sensor's low power  
662 consumption of 8 mW at 5 s sampling intervals and 7 mW at 60 s sampling intervals (Atamanchuk et al., 2014).  
663 Combined with other novel sensors that measure another DIC-related quantity such as  $A_T$  or  $c(\text{DIC})$ ,  $\text{CO}_2$   
664 optodes on gliders could help provide estimates of NCP, air-sea flux, respiration and remineralisation and  
665 aragonite saturation.

666 During our deployment we calculated  $\text{O}_2$  and DIC-based NCP over the spring and summer period. In the future,  
667 extended deployments could be used to estimate annual (full year) NCP. To have an accurate estimate of annual  
668 NCP, at least one additional glider deployment is needed to have continuous coverage (Binetti et al., 2020).  
669 Similar deployments can be used in other areas of the globe to fill gaps in  $N(\text{DIC})$  and  $N(\text{O}_2)$ . In particular, glider  
670 deployments have potential in under-sampled areas of the globe such as the Southern Ocean and the Arctic.  
671 Also, it can be used in well-studied areas such as North and Mediterranean Sea to reduce monitoring costs and  
672 compare NCP estimates with previous studies that used other sampling strategies.

673 *Data availability.* The glider data are available on Norwegian Marine Data Centre (NMDC) at  
674 <https://doi.org/10.21335/NMDC-1654657723>

675

676 *Competing interests.* The authors declare that there is no conflict of interest.

677

678 *Acknowledgements.* Luca Possenti's PhD project is part of the Next Generation Unmanned Systems Science  
679 (NEXUSS) Centre for Doctoral Training which is funded by the Natural Environment Research Council (NERC)  
680 and the Engineering and Physical Science Research Council (EPSRC) [grant number NE/N012070/1]. We would  
681 like to thank the scientists, engineers, and crew that contributed to the glider mission and data collection along  
682 the glider transect and at Ocean Weather Station M (OWSM). We would also like to thank Kristin Jackson-  
683 Misje, who performed all the carbon analyses, as well as Michael Hemming and Bastien Queste for their initial  
684 contributions to the data analysis. We are grateful to the comments from the two anonymous reviewers and the  
685 Editor, which led to a greatly improved paper.

## 686 **6 References**

687 Alkire, M. B., Lee, C., D'Asaro, E., Perry, M. J., Briggs, N., Cetinić, I. and Gray, A.: Net community production  
688 and export from Seaglider measurements in the North Atlantic after the spring bloom, *J. Geophys. Res. Ocean.*,  
689 119(9), 6121–6139, 2014.

690 Anderson, L. A.: On the hydrogen and oxygen content of marine phytoplankton, *Deep sea Res. part I Oceanogr.*  
691 *Res. Pap.*, 42(9), 1675–1680, 1995.

692 Anderson, L. A. and Sarmiento, J. L.: Redfield ratios of remineralization determined by nutrient data analysis,  
693 *Global Biogeochem. Cycles*, 8(1), 65–80, 1994.

694 Atamanchuk, D., Tengberg, A., Thomas, P. J., Hovdenes, J., Apostolidis, A., Huber, C. and Hall, P. O. J.:  
695 Performance of a lifetime-based optode for measuring partial pressure of carbon dioxide in natural waters,  
696 *Limnol. Oceanogr. Methods*, 12(2), 63–73, doi:10.4319/lom.2014.12.63, 2014.

697 Atamanchuk, D., Kononets, M., Thomas, P. J., Hovdenes, J., Tengberg, A. and Hall, P. O. J.: Continuous long-  
698 term observations of the carbonate system dynamics in the water column of a temperate fjord, *J. Mar. Syst.*, 148,

699 272–284, doi:10.1016/j.jmarsys.2015.03.002, 2015a.

700 Atamanchuk, D., Tengberg, A., Aleynik, D., Fietzek, P., Shitashima, K., Lichtschlag, A., Hall, P. O. J. and Stahl,  
701 H.: Detection of CO<sub>2</sub> leakage from a simulated sub-seabed storage site using three different types of pCO<sub>2</sub>  
702 sensors, *Int. J. Greenh. Gas Control*, 38, 121–134, doi:10.1016/j.ijggc.2014.10.021, 2015b.

703 Bakker, D. C. E., Pfeil, B., Landa, C. S., Metzl, N., Brien, K. M. O., Olsen, A., Smith, K., Cosca, C., Harasawa,  
704 S. and Jones, S. D.: A multi-decade record of high-quality fCO<sub>2</sub> data in version 3 of the Surface Ocean CO<sub>2</sub>  
705 Atlas (SOCAT), *Earth Syst. Sci. Data*, 383–413, doi:10.5194/essd-8-383-2016, 2016.

706 Benson, B. B. and Krause Jr, D.: The concentration and isotopic fractionation of oxygen dissolved in freshwater  
707 and seawater in equilibrium with the atmosphere 1, *Limnol. Oceanogr.*, 29(3), 620–632,  
708 <https://doi.org/10.4319/lo.1984.29.3.0620>, 1984.

709 Binetti, U., Kaiser, J., Damerell, G. M., Rummyantseva, A., Martin, A. P., Henson, S. and Heywood, K. J.: Net  
710 community oxygen production derived from Seaglider deployments at the Porcupine Abyssal Plain site (PAP;  
711 northeast Atlantic) in 2012–13, *Prog. Oceanogr.*, 183, 102293, <https://doi.org/10.1016/j.pocean.2020.102293>,  
712 2020.

713 Bittig, H. C. and Körtzinger, A.: Tackling oxygen optode drift: Near-surface and in-air oxygen optode  
714 measurements on a float provide an accurate in situ reference, *J. Atmos. Ocean. Technol.*, 32(8), 1536–1543,  
715 <https://doi.org/10.1175/JTECH-D-14-00162.1>, 2015.

716 Bittig, H. C., Fiedler, B., Steinhoff, T. and Körtzinger, A.: A novel electrochemical calibration setup for oxygen  
717 sensors and its use for the stability assessment of Aanderaa optodes, *Limnol. Oceanogr. Methods*, 10(11), 921–  
718 933, <https://doi.org/10.4319/lom.2012.10.921>, 2012.

719 von Bültzingslöwen, C., McEvoy, A. K., McDonagh, C., MacCraith, B. D., Klimant, I., Krause, C. and  
720 Wolfbeis, O. S.: Sol–gel based optical carbon dioxide sensor employing dual luminophore referencing for  
721 application in food packaging technology, *Analyst*, 127(11), 1478–1483, <https://doi.org/10.1039/B207438A>,  
722 2002.

723 Bushinsky, S. M., Takeshita, Y. and Williams, N. L.: Observing Changes in Ocean Carbonate Chemistry: Our  
724 Autonomous Future, *Curr. Clim. Chang. reports*, 5(3), 207–220, <https://doi.org/10.1007/s40641-019-00129-8>,  
725 2019.

726 Chu, S. N., Sutton, A. J., Alin, S. R., Lawrence-Slavas, N., Atamanchuk, D., Mickett, J. B., Newton, J. A.,  
727 Meinig, C., Stalin, S. and Tengberg, A.: Field evaluation of a low-powered, profiling pCO<sub>2</sub> system in coastal  
728 Washington, *Limnology and Oceanography: Methods*, 18(6), pp.280-296, <https://doi.org/10.1002/lom3.10354>,  
729 2020.

730 Copin-Montégut, C.: Consumption and production on scales of a few days of inorganic carbon, nitrate and  
731 oxygen by the planktonic community: results of continuous measurements at the Dyfamed Station in the  
732 northwestern Mediterranean Sea (May 1995), *Deep Sea Res. Part I Oceanogr. Res. Pap.*, 47(3), 447–477,  
733 [https://doi.org/10.1016/S0967-0637\(99\)00098-9](https://doi.org/10.1016/S0967-0637(99)00098-9), 2000.

734 Degrandpre, M. D.: Measurement of Seawater pCO<sub>2</sub> Using a Renewable-Reagent Fiber Optic Sensor with  
735 Colorimetric Detection, , 1172(8), 331–337, doi:10.1021/ac00052a005, 1993.

736 Dickson, A. G.: Thermodynamics of the dissociation of boric acid in synthetic seawater from 273.15 to 318.15  
737 K, *Deep Sea Research Part A. Oceanographic Research Papers*, 37(5), 755–766, [https://doi.org/10.1016/0198-  
738 0149\(90\)90004-F](https://doi.org/10.1016/0198-0149(90)90004-F), 1990.

739 Dickson, A. G., Afghan, J. D. and Anderson, G. C.: Reference materials for oceanic CO<sub>2</sub> analysis : a method for

740 the certification of total alkalinity, *Marine Chemistry*, 80, 185–197, <https://doi.org/10.1016/S0304->  
741 [4203\(02\)00133-0](https://doi.org/10.1016/S0304-4203(02)00133-0), 2003.

742 Dlugokencky, E. J., Lang, P. M., Masarie, K. A., Crotwell, A. M. and Crotwell, M. J.: Atmospheric carbon  
743 dioxide dry air mole fractions from the NOAA ESRL Carbon Cycle Cooperative Global Air Sampling Network,  
744 1968–2014, NOAA ESRL Glob. Monit. Div. Boulder, CO, USA, 2015.

745 Ducklow, H. W. and Doney, S. C.: What Is the Metabolic State of the Oligotrophic Ocean? A Debate, *Annual*  
746 *Review of Marine Science* 5, doi:10.1146/annurev-marine-121211-172331, 2013.

747 Falck, E. and Anderson, L. G.: The dynamics of the carbon cycle in the surface water of the Norwegian Sea,  
748 *Marine Chemistry*, 94, 43–53, doi:10.1016/j.marchem.2004.08.009, 2005.

749 Falck, E. and Gade, G.: Net community production and oxygen fluxes in the Nordic Seas based on O<sub>2</sub> budget  
750 calculations, *Global Biogeochemical cycles*, 13(4), 1117–1126, <https://doi.org/10.1029/1999GB900030>, 1999.

751 Fiedler, B., Fietzek, P., Vieira, N., Silva, P., Bittig, H. C. and Körtzinger, A.: In situ CO<sub>2</sub> and O<sub>2</sub> measurements  
752 on a profiling float, *J. Atmos. Ocean. Technol.*, 30(1), 112–126, doi:10.1175/JTECH-D-12-00043.1, 2013.

753 Foltz, G. R., Grodsky, S. A., Carton, J. A. and McPhaden, M. J.: Seasonal mixed layer heat budget of the tropical  
754 Atlantic Ocean, *J. Geophys. Res. Ocean.*, 108(C5), <https://doi.org/10.1029/2002JC001584>, 2003.

755 Friedlingstein, P., Jones, M., O’Sullivan, M., Andrew, R., Hauck, J., Peters, G., Peters, W., Pongratz, J., Sitch, S.  
756 and Le Quéré, C.: Global carbon budget 2019, *Earth Syst. Sci. Data*, 11(4), 1783–1838,  
757 <https://doi.org/10.5194/essd-11-1783-2019>, 2019.

758 Garcia, H. E. and Gordon, L. I.: Oxygen solubility in seawater: Better fitting equations, *Limnol. Oceanogr.*,  
759 37(6), 1307–1312, <https://doi.org/10.4319/lo.1992.37.6.1307>, 1992.

760 Gattuso, J.-P. and Hansson, L.: *Ocean acidification*, Oxford University Press., 2011.

761 Gislefoss, J. S., Nydal, R., Slagstad, D., Sonninen, E. and Holme, K.: Carbon time series in the Norwegian sea,  
762 *Deep Sea Research Part I: Oceanographic Research Papers*, 45, 433–460, <https://doi.org/10.1016/S0967->  
763 [0637\(97\)00093-9](https://doi.org/10.1016/S0967-0637(97)00093-9), 1998.

764 Gourcuff, C.: ANFOG Slocum CTD data correction, IMOS, (March), 2014.

765 Goyet, C., Walt, D. R. and Brewer, P. G.: Development of a fiber optic sensor for measurement of pCO<sub>2</sub> in sea  
766 water: design criteria and sea trials, *Deep Sea Res. Part A. Oceanogr. Res. Pap.*, 39(6), 1015–1026, 1992.

767 Hagebo, M. and Rey, F.: Storage of seawater for nutrients analysis, *Fisk. Hav.*, 4, 1, 12,  
768 [https://doi.org/10.1016/0198-0149\(92\)90037-T](https://doi.org/10.1016/0198-0149(92)90037-T), 1984.

769 Hansen, B. and Østerhus, S.: North Atlantic – Nordic Seas exchanges, *Progress in oceanography*, 45, 109–208,  
770 [https://doi.org/10.1016/S0079-6611\(99\)00052-X](https://doi.org/10.1016/S0079-6611(99)00052-X), 2000.

771 Hardman-Mountford, N. J., Moore, G., Bakker, D. C. E., Watson, A. J., Schuster, U., Barciela, R., Hines, A.,  
772 Moncoiffé, G., Brown, J., Dye, S., Blackford, J., Somerfield, P. J., Holt, J., Hydes, D. J. and Aiken, J.: An  
773 operational monitoring system to provide indicators of CO<sub>2</sub>-related variables in the ocean, *ICES J. Mar. Sci.*,  
774 65(8), 1498–1503, doi:10.1093/icesjms/fsn110, 2008.

775 Haskell, W. Z., Hammond, D. E., Prokopenko, M. G., Teel, E. N., Seegers, B. N., Ragan, M. A., Rollins, N. and  
776 Jones, B. H.: Net Community Production in a Productive Coastal Ocean From an Autonomous Buoyancy-Driven  
777 Glider, *J. Geophys. Res. Ocean.*, 124(6), 4188–4207, <https://doi.org/10.1029/2019JC015048>, 2019.

778 Hemsley, J. M.: *OBSERVATIONS PLATFORMS| Buoy*, 2015.

779 Hemsley, V. S., Smyth, T. J., Martin, A. P., Frajka-williams, E., Thompson, A. F., Damerell, G. and Painter, S.  
780 C.: Estimating Oceanic Primary Production Using Vertical Irradiance and Chlorophyll Profiles from Ocean

781 Gliders in the North Atlantic, *49*(19), 11612–11621, doi:10.1021/acs.est.5b00608, 2015.

782 Van Heuven, S., Pierrot, D., Rae, J. W. B., Lewis, E. and Wallace, D. W. R.: MATLAB program developed for  
783 CO<sub>2</sub> system calculations, ORNL/CDIAC-105b. Carbon Dioxide Inf. Anal. Center, Oak Ridge Natl. Lab. US  
784 Dep. Energy, Oak Ridge, Tennessee, 530, 2011.

785 Jeansson, E., Olsen, A., Eldevik, T., Skjelvan, I., Omar, A. M., Lauvset, S. K., Nilsen, J. E. Ø., Bellerby, R. G.  
786 J., Johannessen, T. and Falck, E.: The Nordic Seas carbon budget : Sources , sinks , and uncertainties, *Global*  
787 *Biogeochemical Cycles*, *25*(2002), 1–16, doi:10.1029/2010GB003961, 2011.

788 Kara, A. B., Rochford, P. A. and Hurlburt, H. E.: An optimal definition for ocean mixed layer depth, *J. Geophys.*  
789 *Res. Ocean.*, *105*(C7), 16803–16821, <https://doi.org/10.1029/2000JC900072>, 2000.

790 Kivimäe, C.: Carbon and oxygen fluxes in the Barents and Norwegian Seas: production, air-sea exchange and  
791 budget calculations, PhD Dissertation, University of Bergen, 2007.

792 Klimant, I., Huber, C., Liebsch, G., Neurauder, G., Stangelmayer, A. and Wolfbeis, O. S.: Dual lifetime  
793 referencing (DLR)—a new scheme for converting fluorescence intensity into a frequency-domain or time-  
794 domain information, in *New Trends in Fluorescence Spectroscopy*, pp. 257–274, Springer.,  
795 [https://doi.org/10.1007/978-3-642-56853-4\\_13](https://doi.org/10.1007/978-3-642-56853-4_13), 2001.

796 Körtzinger, A., Thomas, H., Schneider, B., Gronau, N., Mintrop, L. and Duinker, J. C.: At-sea intercomparison  
797 of two newly designed underway pCO<sub>2</sub> systems—encouraging results, *Mar. Chem.*, *52*(2), 133–145,  
798 [https://doi.org/10.1016/0304-4203\(95\)00083-6](https://doi.org/10.1016/0304-4203(95)00083-6), 1996.

799 Körtzinger, A., Koeve, W., Kähler, P. and Mintrop, L.: C: N ratios in the mixed layer during the productive  
800 season in the northeast Atlantic Ocean, *Deep Sea Res. Part I Oceanogr. Res. Pap.*, *48*(3), 661–688,  
801 [https://doi.org/10.1016/S0967-0637\(00\)00051-0](https://doi.org/10.1016/S0967-0637(00)00051-0), 2001.

802 Laws, E. A.: Photosynthetic quotients, new production and net community production in the open ocean, *Deep*  
803 *Sea Res. Part A. Oceanogr. Res. Pap.*, *38*(1), 143–167, [https://doi.org/10.1016/0198-0149\(91\)90059-O](https://doi.org/10.1016/0198-0149(91)90059-O), 1991.

804 Lee, K., Tong, L. T., Millero, F. J., Sabine, C. L., Dickson, A. G., Goyet, C., Park, G. H., Wanninkhof, R., Feely,  
805 R. A. and Key, R. M.: Global relationships of total alkalinity with salinity and temperature in surface waters of  
806 the world’s oceans, *Geophys. Res. Lett.*, *33*(19), 1–5, doi:10.1029/2006GL027207, 2006.

807 Lee, K., Kim, T., Byrne, R. H., Millero, F. J., Feely, R. A. and Liu, Y.: The universal ratio of boron to chlorinity  
808 for the North Pacific and North Atlantic oceans, *Geochim. Cosmochim. Acta*, *74*(6), 1801–1811,  
809 doi:10.1016/j.gca.2009.12.027, 2010.

810 Lockwood, D., Quay, P. D., Kavanaugh, M. T., Juranek, L. W. and Feely, R. A.: High-resolution estimates of  
811 net community production and air-sea CO<sub>2</sub> flux in the northeast Pacific, *Global Biogeochemical Cycles*, *26*, 1–  
812 16, doi:10.1029/2012GB004380, 2012.

813 Lueker, T. J., Dickson, A. G. and Keeling, C. D.: Ocean pCO<sub>2</sub> calculated from DIC, TA, and the Mehrbach  
814 equations for K1 and K2: Validation using laboratory measurements of CO<sub>2</sub> in gas and seawater at equilibrium,  
815 *Abstr. Pap. Am. Chem. Soc.*, 217, U848–U848, 2000.

816 Martz, T. R., Connery, J. G. and Johnson, K. S.: Testing the Honeywell Durafet for seawater pH applications,  
817 *Limnol. Oceanogr. Methods*, *8*, 172–184, doi:10.4319/lom.2010.8.172, 2010.

818 Medeot, N., Nair, R. and Gerin, R.: Laboratory Evaluation and Control of Slocum Glider C – T Sensors, *Journal*  
819 *of Atmospheric and Oceanic Technology*, 838–846, doi:10.1175/2011JTECHO767.1, 2011.

820 Miloshevich, L.: Development and Validation of a Time-Lag Correction for Vaisala Radiosonde Humidity  
821 Measurements, *Journal of Atmospheric and Oceanic Technology*, 1305–1328, 2004.

822 Monteiro, P. M. S., Schuster, U., Hood, M., Lenton, A., Metzl, N., Olsen, A., Rogers, K., Sabine, C., Takahashi,  
823 T. and Tilbrook, B.: A global sea surface carbon observing system: Assessment of changing sea surface CO<sub>2</sub> and  
824 air-sea CO<sub>2</sub> fluxes, *Proc. Ocean.*, 9, 702–714, 2009.

825 Naveira Garabato, A. C., Oliver, K. I. C., Watson, A. J. and Messias, M.: Turbulent diapycnal mixing in the  
826 Nordic seas, *J. Geophys. Res. Ocean.*, 109(C12), <https://doi.org/10.1029/2004JC002411>, 2004.

827 Neftel, A., Oeschger, H., Schwander, J., Stauffer, B. and Zumbunn, R.: Ice core sample measurements give  
828 atmospheric CO<sub>2</sub> content during the past 40,000 yr, *Nature*, 295(5846), 220–223,  
829 <https://doi.org/10.1038/295220a0>, 1982.

830 Neuer, S., Cianca, A., Helmke, P., Freudenthal, T., Davenport, R., Meggers, H. and Knoll, M.: Biogeochemistry  
831 and hydrography in the eastern subtropical North Atlantic gyre . Results from the European time-series station  
832 ESTOC, *Progress in Oceanography*, 72, 1–29, doi:10.1016/j.pocean.2006.08.001, 2007.

833 Nicholson, D., Emerson, S. and Eriksen, C. C.: Net community production in the deep euphotic zone of the  
834 subtropical North Pacific gyre from glider surveys, *Limnol. Oceanogr.*, 53(5 PART 2), 2226–2236,  
835 doi:10.4319/lo.2008.53.5\_part\_2.2226, 2008.

836 Nicholson, D. P. and Feen, M. L.: Air calibration of an oxygen optode on an underwater glider, *Limnol.*  
837 *Oceanogr. Methods*, 15(5), 495–502, doi:10.1002/lom3.10177, 2017.

838 Nilsen, J. E. Ø. and Falck, E.: Variations of mixed layer properties in the Norwegian Sea for the period 1948 –  
839 1999, *Progress in Oceanography*, 70, 58–90, doi:10.1016/j.pocean.2006.03.014, 2006.

840 Obata, A., Ishizaka, J. and Endoh, M.: Global verification of critical depth theory for phytoplankton bloom with  
841 climatological in situ temperature and satellite ocean color data, *J. Geophys. Res. Ocean.*, 101(C9), 20657–  
842 20667, <https://doi.org/10.1029/96JC01734>, 1996.

843 Olsen, A., Key, R. M., Van Heuven, S., Lauvset, S. K., Velo, A., Lin, X., Schirnick, C., Kozyr, A., Tanhua, T.,  
844 Hoppema, M., Jutterström, S., Steinfeldt, R., Jeansson, E., Ishii, M., Pérez, F. F. and Suzuki, T.: The global  
845 ocean data analysis project version 2 (GLODAPv2) - An internally consistent data product for the world ocean,  
846 *Earth Syst. Sci. Data*, 8(2), 297–323, doi:10.5194/essd-8-297-2016, 2016.

847 Osterroht, C. and Thomas, H.: New production enhanced by nutrient supply from non-Redfield remineralisation  
848 of freshly produced organic material, *J. Mar. Syst.*, 25(1), 33–46, [https://doi.org/10.1016/S0924-7963\(00\)00007-](https://doi.org/10.1016/S0924-7963(00)00007-5)  
849 [5](https://doi.org/10.1016/S0924-7963(00)00007-5), 2000.

850 Pachauri, R. K. and Reisinger, A.: IPCC fourth assessment report, IPCC Fourth Assess. Rep., 1, 976 [online]  
851 Available from:  
852 [http://www.construible.es/construible%5Cbiblioteca%5Cpresentacion\\_informe\\_ipcc.pdf%5Cpapers2://publicacion/uuid/DD3ABB67-E411-4C0F-A29C-DA693B95B789](http://www.construible.es/construible%5Cbiblioteca%5Cpresentacion_informe_ipcc.pdf%5Cpapers2://publicacion/uuid/DD3ABB67-E411-4C0F-A29C-DA693B95B789), 2007.

853 Peeters, F., Atamanchuk, D., Tengberg, A.,  
854 Encinas-Fernández, J. and Hofmann, H.: Lake metabolism: Comparison of lake metabolic rates estimated from a  
855 diel CO<sub>2</sub>-and the common diel O<sub>2</sub>-technique, *PLoS One*, 11(12), <https://doi.org/10.1371/journal.pone.0168393>,  
856 2016.

857 Plant, J. N., Johnson, K. S., Sakamoto, C. M., Jannasch, H. W., Coletti, L. J., Riser, S. C. and Swift, D. D.: Net  
858 community production at Ocean Station Papa observed with nitrate and oxygen sensors on profiling floats,  
859 *Global Biogeochem. Cycles*, 30(6), 859–879, <https://doi.org/10.1002/2015GB005349>, 2016.

860 Quay, P., Stutsman, J. and Steinhoff, T.: Primary production and carbon export rates across the subpolar N.  
861 Atlantic Ocean basin based on triple oxygen isotope and dissolved O<sub>2</sub> and Ar gas measurements, *Global*  
862 *Biogeochem. Cycles*, 26(2), <https://doi.org/10.1029/2010GB004003>, 2012.



863 Le Quéré, C., Raupach, M. R., Canadell, J. G., Marland et al., G., Le Quéré et al., C., Le Quéré et al., C.,  
864 Raupach, M. R., Canadell, J. G., Marland, G., Bopp, L., Ciais, P., Conway, T. J., Doney, S. C., Feely, R. A.,  
865 Foster, P., Friedlingstein, P., Gurney, K., Houghton, R. A., House, J. I., Huntingford, C., Levy, P. E., Lomas, M.  
866 R., Majkut, J., Metzl, N., Ometto, J. P., Peters, G. P., Prentice, I. C., Randerson, J. T., Running, S. W.,  
867 Sarmiento, J. L., Schuster, U., Sitch, S., Takahashi, T., Viovy, N., van der Werf, G. R. and Woodward, F. I.:  
868 Trends in the sources and sinks of carbon dioxide, *Nat. Geosci.*, 2(12), 831–836, doi:10.1038/ngeo689, 2009.  
869 Redfield, A. C.: The influence of organisms on the composition of seawater, *The sea*, 2, 26–77, 1963.  
870 Rérolle, V. M. C., Floquet, C. F. A., Harris, A. J. K., Mowlem, M. C., Bellerby, R. R. G. J. and Achterberg, E.  
871 P.: Development of a colorimetric microfluidic pH sensor for autonomous seawater measurements, *Anal. Chim.*  
872 *Acta*, 786, 124–131, <https://doi.org/10.1016/j.aca.2013.05.008>, 2013.  
873 Reuer, M. K., Barnett, B. A., Bender, M. L., Falkowski, P. G. and Hendricks, M. B.: New estimates of Southern  
874 Ocean biological production rates from O<sub>2</sub>/Ar ratios and the triple isotope composition of O<sub>2</sub>, *Deep Sea Res.*  
875 *Part I Oceanogr. Res. Pap.*, 54(6), 951–974, <https://doi.org/10.1016/j.dsr.2007.02.007>, 2007.  
876 Rey, B. F.: 5 . Phytoplankton : the grass of the sea 2001.  
877 Sabine, C. L., Feely, R. A., Gruber, N., Key, R. M., Lee, K., Bullister, J. L., Wanninkhof, R., Wong, C. S. S.,  
878 Wallace, D. W. R., Tilbrook, B., Millero, F. J., Peng, T.-H. T.-H., Kozyr, A., Ono, T., Rios, A. F., A., F. R.,  
879 Gruber, N., Key, R. M., Lee, K., Bullister, J. L., Wanninkhof, R., Wong, C. S. S., Wallace, D. W. R., Tilbrook,  
880 B., Millero, F. J., Peng, T.-H. T.-H., Kozyr, A., Ono, T. and Rios, A. F.: The oceanic sink for anthropogenic  
881 CO<sub>2</sub>, *Science* ., 305(5682), 367–371, doi:10.1126/science.1097403, 2004.  
882 Saderne, V., Fietzek, P. and Herman, P. M. J.: Extreme Variations of pCO<sub>2</sub> and pH in a Macrophyte Meadow of  
883 the Baltic Sea in Summer: Evidence of the Effect of Photosynthesis and Local Upwelling, *PLoS One*, 8(4), 2–9,  
884 doi:10.1371/journal.pone.0062689, 2013.  
885 Saetre, R. and Ljoen, R.: THE NORWEGIAN COASTAL CURRENT, 1972.  
886 Seguro, I., Marca, A. D., Painting, S. J., Shutler, J. D., Suggett, D. J. and Kaiser, J.: High-resolution net and  
887 gross biological production during a Celtic Sea spring bloom, *Prog. Oceanogr.*, 177, 101885,  
888 <https://doi.org/10.1016/j.pocean.2017.12.003>, 2019.  
889 Seidel, M. P., Degrandpre, M. D. and Dickson, A. G.: A sensor for in situ indicator-based measurements of  
890 seawater pH, *Marine chemistry*, 109, 18–28, doi:10.1016/j.marchem.2007.11.013, 2008.  
891 Sharples, J., Ross, O. N., Scott, B. E., Greenstreet, S. P. R. and Fraser, H.: Inter-annual variability in the timing  
892 of stratification and the spring bloom in the North-western North Sea, *Cont. Shelf Res.*, 26(6), 733–751,  
893 <https://doi.org/10.1016/j.csr.2006.01.011>, 2006.  
894 Skjelvan, I., Falck, E., Anderson, L. G. and Rey, F.: Oxygen fluxes in the Norwegian Atlantic Current, *Mar.*  
895 *Chem.*, 73(3–4), 291–303, doi:10.1016/S0304-4203(00)00112-2, 2001.  
896 Skjelvan, I., Anderson, L. G., Falck, E. and Anders, K.: A Review of the Inorganic Carbon Cycle of the Nordic  
897 Seas and Barents Sea , 2005.  
898 Skjelvan, I., Falck, E., Rey, F. and Kringstad, S. B.: Inorganic carbon time series at Ocean Weather Station M in  
899 the Norwegian Sea, *Biogeosciences*, 549–560, <https://doi.org/10.5194/bg-5-549-2008>, 2008.  
900 Sprintall, J. and Roemmich, D.: Characterizing the structure of the surface layer in the Pacific Ocean, *J.*  
901 *Geophys. Res. Ocean.*, 104(C10), 23297–23311, <https://doi.org/10.1029/1999JC900179>, 1999.  
902 Sutton, A. J., Sabine, C. L., Meinig, C. and Feely, R. A.: A high-frequency atmospheric and seawater p CO<sub>2</sub>  
903 data set from 14 open-ocean sites using a moored autonomous system, *Earth System Science Data*, 353–366,  
904 doi:10.3334/CDIAC/OTG.TSM, 2014.

905 Swift, J. H.: The arctic waters, in *The Nordic Seas*, pp. 129–154, Springer., 1986.

906 Takahashi, T., Sutherland, S. C., Sweeney, C., Poisson, A., Metzl, N., Tilbrook, B., Bates, N., Wanninkhof, R.,  
907 Feely, R. A., Sabine, C., Olafsson, J. and Nojiri, Y.: Global sea – air CO<sub>2</sub> flux based on climatological surface  
908 ocean pCO<sub>2</sub>, and seasonal biological and temperature effects, *Deep Sea Research Part II: Topical Studies in*  
909 *Oceanography*, 49, 1601–1622, [https://doi.org/10.1016/S0967-0645\(02\)00003-6](https://doi.org/10.1016/S0967-0645(02)00003-6), 2002.

910 Takahashi, T., Sutherland, S. C., Wanninkhof, R., Sweeney, C., Feely, R. A., Chipman, D. W., Hales, B.,  
911 Friederich, G., Chavez, F., Sabine, C., Watson, A., Bakker, D. C. E., Schuster, U., Yoshikawa-Inoue, H., Ishii,  
912 M., Midorikawa, T., Nojiri, Y., Körtzinger, A., Steinhoff, T., Hoppema, M., Olafsson, J., Arnarson, T. S.,  
913 Johannessen, T., Olsen, A., Bellerby, R., Wong, C. S., Delille, B., Bates, N. R. and de Baar, H. J. W.:  
914 Climatological mean and decadal change in surface ocean pCO<sub>2</sub>, and net sea–air CO<sub>2</sub> flux over the global  
915 oceans, *Deep Sea Res. Part II Top. Stud. Oceanogr.*, 56(8), 554–577, doi:10.1016/j.dsr2.2008.12.009, 2009.

916 Tengberg, A., Hovdenes, J., Andersson, H. J., Brocandel, O., Diaz, R. and Hebert, D.: Evaluation of a lifetime-  
917 based optode to measure oxygen in aquatic systems, *OCEANOGRAPHY : METHODS*, (1964), 7–17,  
918 <https://doi.org/10.4319/lom.2006.4.7>, 2006.

919 Thomas, H., Ittekkot, V., Osterroht, C. and Schneider, B.: Preferential recycling of nutrients—the ocean’s way to  
920 increase new production and to pass nutrient limitation?, *Limnol. Oceanogr.*, 44(8), 1999–2004,  
921 <https://doi.org/10.4319/lo.1999.44.8.1999>, 1999.

922 Thomas, P. J., Atamanchuk, D., Hovdenes, J. and Tengberg, A.: The use of novel optode sensor technologies for  
923 monitoring dissolved carbon dioxide and ammonia concentrations under live haul conditions, *Aquac. Eng.*, 77,  
924 89–96, <https://doi.org/10.1016/j.aquaeng.2017.02.004>, 2017.

925 Thompson, R. O. R. Y.: Climatological numerical models of the surface mixed layer of the ocean, *J. Phys.*  
926 *Oceanogr.*, 6(4), 496–503, 1976.

927 United States. National Environmental Satellite and Information Service, D., Monterey, G. I. and Levitus, S.:  
928 Seasonal variability of mixed layer depth for the world ocean, US Department of Commerce, National Oceanic  
929 and Atmospheric Administration . . . ., 1997.

930 Wanninkhof, R.: Relationship between wind speed and gas exchange over the ocean revisited,  
931 *OCEANOGRAPHY : METHODS*, 351–362, doi:10.4319/lom.2014.12.351, 2014.

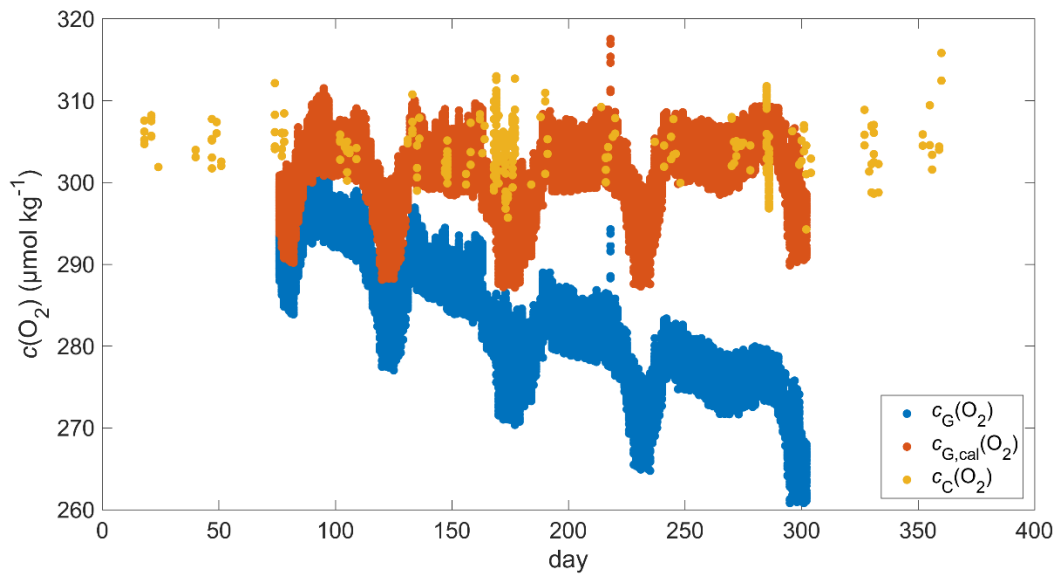
932 Weiss, R. F.: Carbon dioxide in water and seawater: the solubility of a non-ideal gas, *Mar. Chem.*, 2(3), 203–  
933 215, doi:10.1016/0304-4203(74)90015-2, 1974.

934 Weiss, R. F. and Price, B. A.: Nitrous oxide solubility in water and seawater, *Mar. Chem.*, 8(4), 347–359,  
935 [https://doi.org/10.1016/0304-4203\(80\)90024-9](https://doi.org/10.1016/0304-4203(80)90024-9), 1980.

936 Woolf, D. K. and Thorpe, S. A.: Bubbles and the air-sea exchange of gases in near-saturation conditions, *J. Mar.*  
937 *Res.*, 49(3), 435–466, <https://doi.org/10.1357/002224091784995765>, 1991.

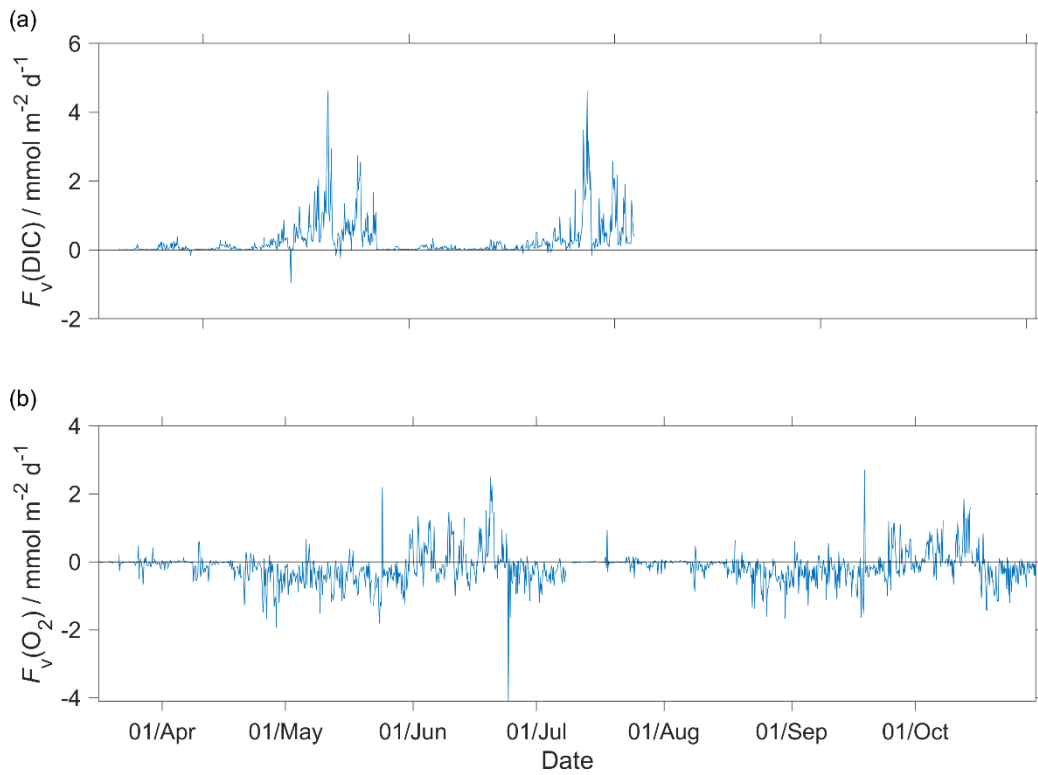
938

## 939 7 Appendices



940

941 **Figure A1:** Discrete samples  $c_C(\text{O}_2)$  (yellow), raw glider oxygen  $c_G(\text{O}_2)$  (blue) and drift corrected glider oxygen  
 942  $c_{G,\text{cal}}(\text{O}_2)$  (red) for a potential density  $> 1028 \text{ kg m}^{-3}$  at depths less than 1000 m.



943

944 **Figure A2:** Diapycnal mixing ( $F_v$ ) calculated for the glider descent and ascent for a)  $c(\text{DIC})$  and b)  $\text{O}_2$  at the  
 945 mixed layer depth ( $z_{\text{mix}}$ ) when deeper than 45 m ( $z_{\text{lim}}$ ) and at  $z_{\text{lim}}$  when  $z_{\text{mix}}$  was shallower than 45 m. In the  
 946 calculations we used a vertical eddy diffusivity ( $K_z$ ) of  $10^{-5} \text{ m}^2 \text{ s}^{-1}$  (Naveira Garabato et al., 2004).